The formation of the giant Huayangchuan U-Nb deposit associated with carbonatite in the Qingling Orogenic Belt

Shuo Xue[a,i], Ming-Xing Ling[b,*], Yu-Long Liu[c], Qing-Qing Kang[d], Rui-Fang Huang[e], Zhe-Kun Zhang[a,i], Weidong Sun[f,g,h,i]

[a] State Key Laboratory of Isotope Geochemistry, Guangzhou Institute of Geochemistry, Chinese Academy of Sciences, Guangzhou 510640, China
[b] State Key Laboratory of Nuclear Resources and Environment, East China University of Technology, Nanchang 330013, China
[c] CAS Key Laboratory of Mineralogy and Metallogeny, Guangzhou Institute of Geochemistry, Chinese Academy of Sciences, Guangzhou 510640, China
[d] Team 224 of Sino Shaanxi Nuclear Industry Group, Xi'an 710100, China
[e] SUSTech Academy for Advanced Interdisciplinary Studies, Southern University of Science and Technology, Shenzhen 518055, China
[f] Center of Deep Sea Research, Institute of Oceanography, Chinese Academy of Sciences, Qingdao 266071, China
[g] Laboratory for Marine Mineral Resources, Qingdao National Laboratory for Marine Science and Technology, Qingdao 266237, China
[h] Center for Ocean Mega-Science, Chinese Academy of Sciences, Qingdao 266071, China
[i] University of Chinese Academy of Sciences, Beijing 100049, China

ARTICLE INFO

ABSTRACT

Carbonatitic magmatism plays a significant role in outgassing carbon from mantle and the formation of rare earth element (REE), rare metal (e.g., Nb and Th) and other types of deposits. The mechanism of REE mineralization associated with carbonatite have been widely studied. However, it is hard to understand U-Nb mineralization without Th enrichment associated with carbonatite. Here we report a carbonatite-hosted U-Nb deposit in Huayangchuan, located in the north Qinling Orogenic Belt. Field observation, mineralogy and geochemical analysis on a suite of drillhole samples were conducted to decipher the mineralization mechanism and its relationship with carbonatite. Huayangchuan carbonatite samples mainly consist of calcite and augite with small volume of accessory minerals (e.g., allanite, fluorapatite, barite and celestite). Betafite $[(Ca,U)_2(Ti,Nb,Ta)_2O_6(OH)]$ is the major ore-bearing mineral in Huayangchuan deposit.

The carbonatite shows high CaO, low MgO and alkali contents, which should be products to be differentiated from primary carbonatite (high MgO and alkali contents). The immiscibility and crystallization processes could explain the high CaO/(CaO + MgO + FeO) ratios and the enrichment of LILE. Numerical modeling also indicates positive $\delta^{18}O_{SMOW}$ (7.29 to 15.53‰) and negative $\delta^{13}C_{PDB}$ (−5.26 to −10.08‰) shifts are induced by reduced sediments assimilation from source consistent with there being enriched Sr-Nd and low Mg isotopic compositions. LA-ICP-MS zircon U-Pb dating of Huayangchuan carbonatite yielded Triassic ages of 229 ± 3 Ma, which corresponds to the post-collision stage of Qinling Orogen during the middle-late Triassic. We then proposed that the recycling of subducted sediments and later re-melting of those materials in shallow mantle generated the Huayangchuan carbonatite and subsequently formed the Huayangchuan deposit. Fluorine concentration decrease, caused by fluorapatite crystallization, ultimately resulted in betafite mineralization.

1. Introduction

Carbonatite is a type of rare but economically important rock, which is generally associated with light rare earth elements (LREE) and rare metal deposit. As reported, about 527 carbonatite intrusions or extrusions are distributed in various geological settings (Woolley and Kjarsgaard, 2008). Among them, nearly 20% of carbonatites display characteristics of geochemical enrichments in rare metal and LREE (Mariano, 1989; Woolley and Kjarsgaard, 2008; Hou et al., 2015). For example, Bayan Obo is the largest LREE deposit in the world, as well as a large iron, niobium and thorium deposit in China (Fan et al., 2016; Lai et al., 2012; Ling et al., 2013; Liu et al., 2018; Yang et al., 2017; Yang et al., 2009; Yuan et al., 1992). The mechanisms of REE mineralization associated with carbonatite have been well constrained by previous researches (Smith and Henderson, 2000; Ling et al., 2013; Doroshkevich et al., 2009; Chakhmouradian and Zaitsev, 2012).
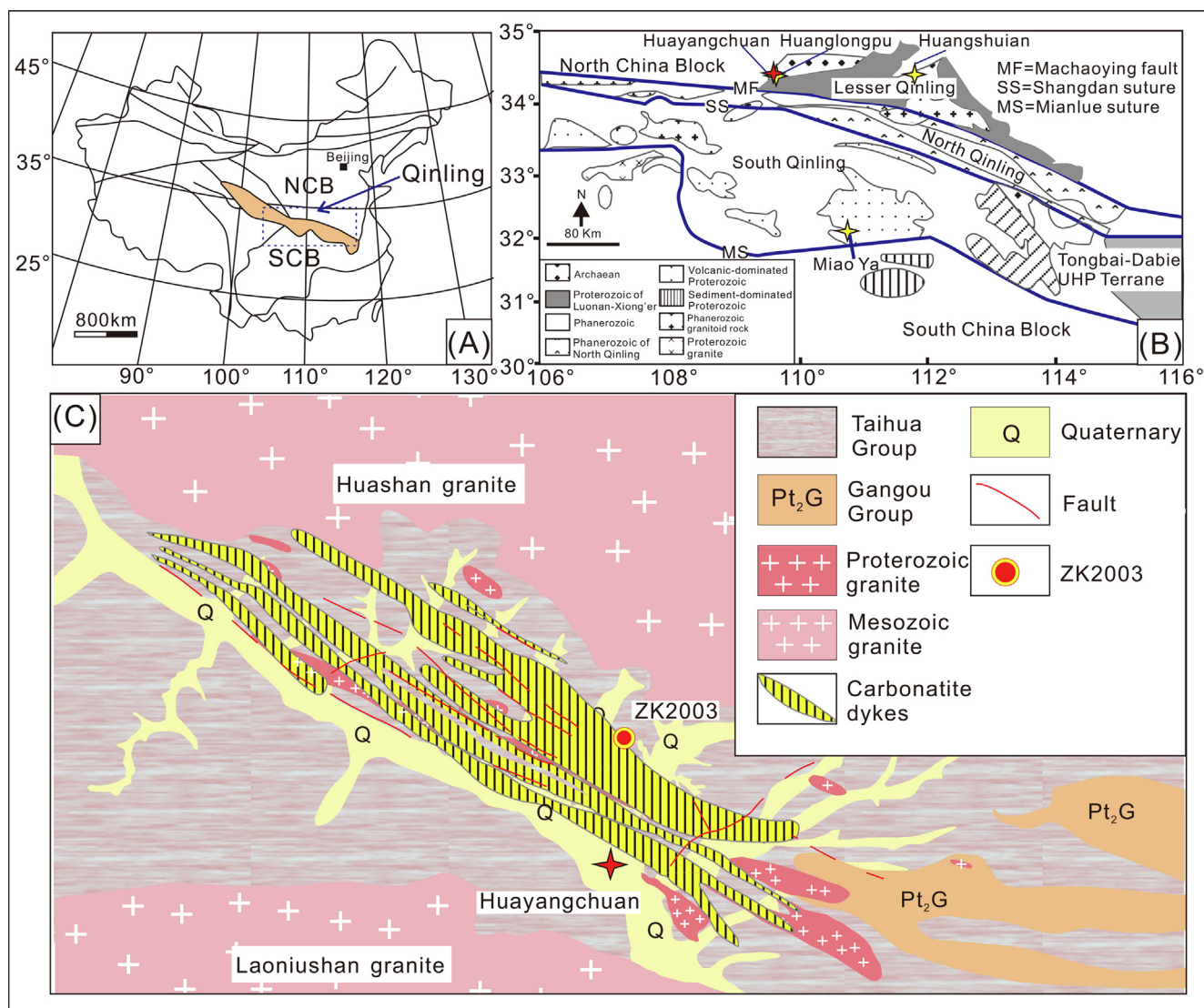

Fig. 1. (A) Tectonic subdivisions of China (Xia et al., 2012). (B) Geological map of the Lesser Qinling district. Four carbonatite dykes with distinct mineralizations. Huayangchuan: U-Nb; Huanglongpu and Huangshuian: Mo; Miaoya: LREE. (C): Geological map of the Huayangchuan ore district.

However, other kinds of mineralization (e.g., U and Nb) is also rarely reported among all carbonatite worldwide, e.g., Tamil Nadu and Rajasthan in India, Ndale in Uganda and Oka in Canada and Lofdal in Namibia (Gaudet, 2013; Viladkar and Ghose, 2002; Dahlkamp, 1978; Hogarth and Horne, 1989; Petruk and Owens, 1975), among which the ore-forming mechanism remains controversial.

Here we report a carbonatite-hosted U-Nb deposit in Huayangchuan, which is located at the Lesser Qinling area, at the southern margin of the NCC (Fig. 1). Prior researches on Huayangchuan U-Nb deposit focused on petrogenesis, geochronology and mineralization mechanism (Gao et al., 2017; Gao et al., 2015; He et al., 2016; Hui et al., 2017; Hui and He, 2016; Song et al., 2016; Xu et al., 2007; Xu et al., 2011; Yu, 1992). However, many controversies still exist recently. Although REE and Nb mineralizations are closely related with carbonatite, U enrichment is commonly associated with granitic melts. Therefore, some researchers have suggested the mineralization was mainly controlled by pegmatite magmatism. While others proposed that the ore-forming materials had been carried by carbonatitic melts.

To date, the ages of Huayangchuan carbonatite and its mineralization still continue to be debated. Molybdenite Re–Os dating and the Monazite U-Pb dating of the North Qinling carbonatite plutons give Late Triassic ages of 209–221.5 Ma (Song et al., 2016; Du et al., 2004;

Stein et al., 1997; Sun et al., 2002). Still, these ages are different from what is found on recent biotite Ar-Ar age (132–133 Ma) of Huayangchuan carbonatite (He et al., 2016). More precise dating work should be performed on the Huayangchuan carbonatite, especially zircon U-Pb dating. In addition, the Huayangchuan carbonatites have low Mg isotopic characteristics ($-1.89 \sim -1.07$‰), high ($^{87}Sr/^{86}Sr)_i$ values (> 0.70495), varied ε_{Nd} values ($-4.3 \sim -10.1$) and also extremely high LILEs (Sr, Ba, U and Pb) concentrations (Song et al., 2016; Xu et al., 2010). It is still unclear what mechanism may have contributed to these specific isotopic and trace element characteristics.

In the Huangyangchuan district, Nb and U are mainly enriched in betafide [$(Ca,U)_2(Ti,Nb,Ta)_2O_6(OH)$]. Moreover, the precipitation mechanism of betafide is still obscure. Some authors suggested betafide formed in the granitic pegmatite (Gao et al., 2015). Others indicated carbonatite is main ore-bearing rock (Hui et al., 2017). However, there is still unclear as to when betafide have formed, as to whether during a magmatic stage or late hydrothermal stage (Gao et al., 2017; He et al., 2016; Hui and He, 2016). Within this contribution, detailed field observation, mineralogy, whole-rock major and trace element, carbonate C and O isotopic analysis, zircon U-Pb dating and chemical mapping of betafite on a suite of drillhole samples were conducted to decipher genesis of carbonatite and the ore-forming mechanism in question.

2. Tectonic background

The Qinling orogenic belt is divided into four sub-units from north to south (Fig. 1a): Lesser Qinling, North Qinling Belt (NQB), South Qinling Belt (SQB), separated by Shangdan suture and Mianlue suture, respectively. Lesser Qinling is the northernmost part of the North Qinling Belt, which adjoins the NCC to the north (Fig. 1b). Previous studies suggested that the Qinling Orogen experienced a prolonged continental divergence and convergence between the North China and South China blocks (Meng and Zhang, 2000; Sun et al., 2002; Xue et al., 1996).

During the period from Late Neoproterozoic to Early Paleozoic, the South Qinling and North Qinling were still the margins of the South China and the North China blocks, separated by the Shangdan Ocean (Meng and Zhang, 2000). The Shangdan Ocean likely existed during Early Silurian and was finally closed prior to Middle Devonian (Dong et al., 2011). The North Qinling evolved into an active margin when the Shangdan ocean subducted northward during the Ordovician. Collision of the South and North Qinling having taken place during Middle Paleozoic along the Shangdan suture (Sun et al., 2002; Zhang et al., 1996). At the same time as collision, extension began from Mid-Devonian, and thereby the Mianlue basin developed within the northern margin of the South China block, the following occurred. The Mianlue oceanic crust suffered northward subduction beneath the South Qinling Belt from Permian to Early Triassic (Sun et al., 2002; Zhang et al., 1996; Meng and Zhang, 2000). Collision of the South Qinling and the South China block came about in the Late Triassic along the Mianlue suture. The Late Triassic collisional orogeny caused extensive fold-and-thrust deformation and granitoid intrusions throughout the Qinling, leading to final amalgamation of the North and South China blocks (Dong et al., 2011).

Carbonatites are extensively developed in the Qinling Orogen, e.g., Huayangchuan, Huanglongpu, Huangshuian and Miaoya. Among them, Huayangchuan, Huanglongpu and Huangshuian carbonatite veins are situated in the Lesser Qinling from west to east (Song et al., 2016; Xu et al., 2011). Miaoya carbonatite lies in the South Qinling Belt (Xu et al., 2010). These carbonatites are all calcio-carbonatites, while displaying distinct mineralization types. The Huayangchuan carbonatite show U-Nb mineralization (Gao et al., 2017). The Huanglongpu and Huangshuian carbonatites contain abundant molybdenite and, it is evident, formed a large Mo deposit (Cao et al., 2014; Song et al., 2015). While the Miaoya carbonatite rocks contain economic LREE ores (Xu et al., 2010).

3. Geological background of the Huayangchuan ore district

The Huayangchuan U-Nb deposit, which occupies an area of 50 km^2, is located at the western Lesser Qinling district (Gao et al., 2017). In Huayangchuan U-Nb deposit district, the Taihua Group gneiss is the oldest crystalline basement in the Huayangchuan district, which has 2.2–2.6 Ga crystallization age and 1.8–1.9 Ga metamorphic age (Xu et al., 2009). The major fault trends NWW, but while aligned with multiple NE trending secondary faults. The extensively developed faults provide profitable space for later magmatism and mineralization (Fig. 1c). Multistage magmatic and metamorphic events were developed in the Lesser Qinling terrane since the crystalline basement formation (Taihua Group). The ~1.8 Ga granite porphyry and the pegmatite dykes cut a suite of Taihua Group gneiss with NWW trending (Fig. 2). The granite porphyry pluton is characterized of A$_1$-type granite, corresponding to the Paleoproterozoic multi-stage rift events at ~1836 Ma (Xue et al., 2018b). However, the pegmatite dykes have not been reported by detailed petrology, mineralogy and geochronology studies.

Carbonatite is the mainly ore-bearing rock, cutting the Taihua Group genesis, pegmatite and granite porphyry (Song et al., 2016; Xu et al., 2007; Xu et al., 2011; Xue et al., 2018b). The carbonatite dykes are dominated by calcite with typical individual crystals ranging from < 0.1 cm to 2 cm in size. Quartz-calcite veins are the most widely distributed ore bearing veins in the region, consisting of quartz (> 50%), calcite (30–40%,), barite, and minor plagioclase. Calcite carbonatite dykes at Huayangchuan extend from 0.1–1 m to ~10 m. Most of dykes predominantly dips N to NNW at steep angles. The trend of carbonatite dykes is controlled by the super-deep local Xiaohe fault.

Triassic Wengyu adakitic granite is suited at the northern part of Huayangchuan ore deposit, which then could mean that it is the melting product of what is thickened low continental crust at ~205 Ma (Hu et al., 2012). The Huashan and Laoniushi granite intrusions were the last and strongest magmatic events to have been within the Huayangchuan ore district, distributed between northern and south parts of the ore deposit, respectively. Previous researchers have suggested that these two granite plutons formed at the 136 Ma and 140 Ma, respectively (Ding et al., 2011; Hu et al., 2012).

In general, the Huayangchuan deposit has the characteristics of large scale, relatively low-grade of uranium. Betafite is the main Nb-U mineral in the deposit, accompanied by calcite, aegirine-augite, allanite, fluorapatite, barite and celestite minerals. The Se (8.98 ppm, 5826 t) and SrSO$_4$ (4%, 28 Mt) reserves belong to giant ore types according to the classification of international standard. Huayangchuan deposit contains Nb (0.019%, 111 kt), Pb (0.68%, 2.18 Mt), Ag (6.24 ppm, 4310 t), Bi (90.36 ppm, 62596 t), REE (0.085%, 550 kt), BaSO$_4$ (3.79%, 2.71 Mt), S (1.56%, 1.01 Mt) (Gao et al., 2017). We collected 161 drillhole samples from the Huayangchuan drillhole (ZK2003) in the main mining area. Detailed mineralogical and geochemical study has been performed in order to analyze what lithology, alteration mineralogy and mineralization is relevant.

4. Analytical methods

4.1. Whole rock major and trace element analyses

Fresh drillhole samples were ground to 200 mesh for major and trace element analysis. Analyses of major and trace elements were performed at the State Key Laboratory of Isotope Geochemistry, Guangzhou Institute of Geochemistry, Chinese Academy of Sciences (SKLIG-GIGCAS). Powder samples was fluxed with Li$_2$B$_4$O$_7$ (1:8) to make homogeneous glass disks at 1150–1200 °C using a V8C automatic fusion machine (Analymate, China). Major elements were determined by Rigaku 100e XRF with analytical precision recorded at superior to 1%. The sample powders were dissolved in Teflon beakers for 7 days at 100 °C using HF + HNO$_3$. For trace element analyses, about 40 mg powders of each sample were accurately weighed and dissolved by a HF and HNO$_3$ mixture in screw-top Teflon beakers at 120 °C in a clean laboratory. Sample solutions were dried and diluted to 3% HNO$_3$ with a factor of 1/2000. Rh was used as an internal standard for calibration. The trace elements of these samples were analyzed using an ICP-MS of Agilent 7700x with precision rate better than 5% (Liu et al., 1996). Table A1 provides the results for findings regarding both the major and trace elements involved.

4.2. SIMS zircon oxygen isotope analysis

Zircons were separated from samples by traditional heavy liquid and magnetic separation techniques, as handpicked under a binocular microscope, mounted with epoxy resin and then polished down to near half sections to expose internal structures for SIMS analyses. Cathodoluminescence (CL) images were used to inspect the zircon morphology; the clearest, least fractured rims of the zircon crystals were selected as suitable targets. Zircon oxygen isotopes were measured using the Cameca IMS-1280 SIMS at the SKLIG-GIGCAS. Measurements were made using a primary beam of ^{133}Cs$^+$ ions accelerated at 10 kV, with an intensity of ~2 nA, rasterized over a 10 μm area. An electron flood gun was used for charge compensation during analysis. Oxygen
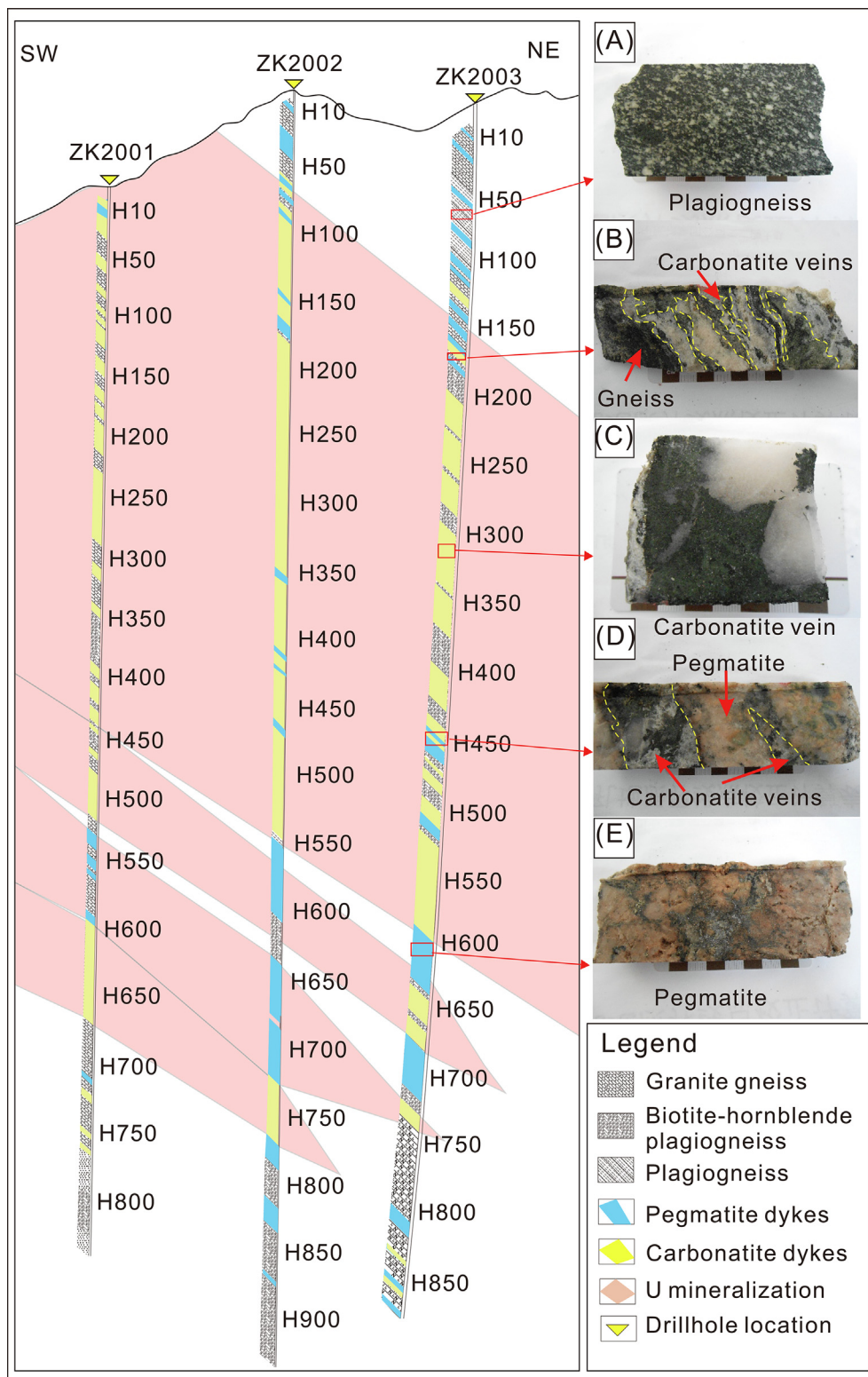
Fig. 2. Section diagram of the 20st drillhole survey line. A: Plagiogneiss; B: Plagiogneiss cutting by the carbonatite veins; C: Carbonatite veins including: calcite and aegirine-augite; D: pegmatite cutting by carbonatite veins; E: granite pegmatite dykes.

isotopes, ^{18}O and ^{16}O, were measured simultaneously in multi-collector mode using two off-axis Faraday cups. Measured $^{18}O/^{16}O$ ratios were normalized by using Vienna Standard Mean Ocean Water (V-SMOW). The detailed analytical procedures were similar to those described by Li et al. (2010). The measured oxygen isotopic data were corrected for instrumental mass fractionation using the "Qinghu" and "Penglai"

zircon standard (Li et al., 2010). The internal precision of a single analysis generally was better than 0.2‰ (1σ standard error) for the $^{18}O/^{16}O$ ratio. The external precision, measured by the reproducibility of repeated analyses of Penglai standard is 0.50‰ (2SD, n = 68). Zircon from carbonatite samples (CT07 and CT09) were selected to perform O isotope analysis (Table A2).

4.3. Zircon U–Pb dating

The zircon U–Pb dating was carried out by LA–ICP–MS at SKLIG-GIGCAS, applying a laser energy rate of 80 mJ, a repetition rate of 8 Hz, spot size (diameter) of 33 μm, and ablation time of 40 s. Helium was used as the carrier gas to enhance the transport efficiency of the ablated material. NIST SRM610 and TEMORA were used as external calibration standards and analyzed twice every 10 analyses; ^{29}Si was employed as an internal standard to calculate the trace element concentrations (Li et al., 2012; Liang et al., 2009; Tu et al., 2011). The isotope ratios and trace element contents were calculated from the raw data using ICPMSDataCal 7.2 (Lin et al., 2016; Liu et al., 2009; Liu et al., 2008). Concordia diagrams were constructed using Isoplot 3.0 (Ludwig, 2012). A more detailed description of the methods can be found in Lin et al. (2016). Carbonatite (CT-07 and CT-09) and pegmatite samples (HGWJ-13, HGWJ-14 and HGWJ-15) were selected to conduct the zircon U-Pb dating (Table A3).

4.4. Whole rock carbon and oxygen isotope analysis

Drillhole samples were analyzed for $^{13}C/^{12}C$ and $^{18}O/^{16}O$ at the Institute of Earth Environment, Chinese Academy of Sciences (IEECAS) using an isotope ratio mass spectrometer (MAT-252) with an automated carbonate preparation device (Kiel II) (Liu et al., 2009). Results are expressed in delta (δ) notation relative to the V-PDB standard. Repeated analyses of laboratory standard carbonates with known $\delta^{13}C$ and $\delta^{18}O$ values were carried out daily to ensure instrumental accuracy. The analytical error of the laboratory standard was approximately ± 0.1‰ for $\delta^{13}C$. The analytical error is approximately ± 0.2‰ for $\delta^{18}O$. The results of C-O isotopic compositions are listed in the Table A4.

4.5. Chemical mapping of minerals using electron microprobe and LA-ICP-MS

High resolution X-ray major element mapping for Nb, Ti, U, Ca, P, F, Cl were applied for betafite grains on carbon-coated thin sections. The X-ray mapping was carried out using a JEOL JXA-8230 electron microprobe at the Key Laboratory of Mineralogy and Metallogeny in GIGCAS. The operation conditions of an accelerate voltage of 20 kV, a probe current of 20 nA and a beam size of 5 μm were adopted for mapping. The step size varied from 5 μm and the dwell time was set to be 100 ms for each point (Xing et al., 2017).

LA-ICP-MS trace element mapping was performed in Ore deposit and Exploration Centre (ODEC), Hefei University of Technology, using a laser ablation system, coupled to a quadrupole-based ICP-MS (Agilent 7900) (Ning et al., 2017). A beam size of 15–40 μm and scan speeds of 15–40 μm/s (equal to beam size) were chosen in this study. A laser repetition of 10 Hz was selected at a constant energy output of 50 mJ, resulting in an energy density of ~5 J/cm² at the target. A 20 s background acquisition happened at the outset doing the scanning. In order to allow for cell wash-out, gas stabilization, and computer processing, a delay of 20 s was used after ablation. Reference materials NIST-610 or GSE-1G at the start and end of each mapping was analyzed for data calibration. Images were compiled and processed using the program LIMS (Wang et al., in press). For each raster and every element, the average background was subtracted from its corresponding raster, and the rasters were then compiled into a 2D image, displaying combined background/drift corrected intensity for each element (Wang et al., 2017).

4.6. In situ trace element analysis of minerals

LA-ICP-MS in situ trace elements of apatite, betafite, calcite and aegirine-augite were measured by LA-ICP-MS on polished thick thin sections at the ODEC, Hefei University of Technology. The analyses were carried out on an Agilent 7900 Quadrupole ICP-MS coupled to a Photon Machines Analyte HE 193 nm ArF Excimer Laser Ablation system equipped. A squid signal smoothing device is included in this laser ablation system. Helium was applied as a carrier gas. Argon was used as the make-up gas and mixed with the carrier gas via a T-connector before entering the ICP (Ning et al., 2017; Wang et al., 2017).

Each analysis was performed by a uniform spot size diameter of 30 mm at 8 Hz with energy of ~ 4 J/cm² for 40 s after measuring the gas blank for 20 s. Standard reference materials BCR-2G, NIST 610 and NIST 612 were used as external standards to plot calibration curve. The off-line data processing was performed using a program called ICPMSDataCal (Liu et al., 2008). Analytical errors for mineral trace elements are at a rate of 10%.

5. Results

5.1. Drillhole samples lithology and geochemistry

Three main rock types are identified from the drillhole samples: (1) Taihua Group gneiss, mainly including biotite plagiogneiss and granite gneiss, (2) granite pegmatite dykes, and (3) carbonatite. Late carbonatite dykes cut the ancient gneiss and pegmatite dykes, so they could be clearly observed in the field and drillhole samples (Fig. 2).

The crystallization basement of Huayangchuan is a set of Paleoproterozoic Taihua Group gneiss, which is a suite of medium- to high-grade metamorphic rocks consisting of mostly banded biotite gneisses and a few granitic gneisses. The representative biotite gneiss shows a granoblastic micro texture and gneissic foliation. It is composed of plagioclase (60–65%), quartz (10–15%), biotite (15–20%), amphibole (5–10%), minor potassium feldspar and alteration mineral (such as chlorite, tremolite and sericite) (Fig. 3A and B). Amphibole and feldspar are extensively altered into chlorite and sericite, respectively. The gneisses are enriched in LILE (Sr, Ba, Rb) and LREE, but are depleted in HREE and high field strength element (HFSE, e.g., Nb and Ta) (Fig. 4A and B).

The pegmatite dykes were broadly outcropped in the Taihua gneiss with NWW direction and at a NNE inclination (blue region in Fig. 2). The granite pegmatite dykes mainly consist of coarse quartz, plagioclase and K-feldspar (mineral grains size: 0.5–1.5 cm, Fig. 3C and D). The pegmatite dykes show high LILE (Sr, Ba, Rb) and LREE, depleted in HREE and HFSE (Nb and Ta), which are similar with the Taihua gneiss (Fig. 4C and D). Pure pegmatite dykes without later alterations show no clear U-Nb enrichment. The pegmatite dykes may be formed out of the anatexis magma of the Taihua gneiss. High precision zircon LA-ICP-MS U-Pb dating of HGWJ-14 and HGWJ-15 yield a Paleoproterozoic crystallization age of 1794 Ma and 1808 Ma, respectively (Fig. 5a and b).

The carbonatite dykes intruded into the Taihua gneiss at the depth of 150 to 600 m, consistent with higher CaO contents and large volume calcites taken from among drilling samples (Fig. 6). The extensive carbonate dykes have mainly consisted of calcite, aegirine-augite, allanite, apatite, sphene, phlogopite, celestite-barite and zeolite (Fig. 3E-J). The U-Nb enrichments also developed at the depth of 150 to 600 m, which is also consistent with given development of carbonatite dykes (Fig. 6). The Huayangchuan carbonatite is a typical calcio-carbonatite. The carbonatites have obvious positive Ba, Sr, U and Nb anomalies and negative Zr and Hf anomalies, consistent with the standard characteristics of global carbonatites. However, the relative flat REE feature and enriched Sr-Nd-Pb isotopic characteristics, distinctive, regarding typical carbonatites worldwide (extreme enrichment of LREE) (Fig. 4E and F). Most C–O isotopic compositions of the carbonatite samples fall within the range of what are primary carbonatites (−8 to −4% and 6 to 10%, Taylor et al., 1967). However, there still are several carbon and oxygen isotope composition of calcite plots outside the mantle field (Fig. 7). Precise zircon LA-ICP-MS U-Pb dating reveals Huayangchuan carbonatite dykes were formed in the Triassic age of 230 Ma (Fig. 5c).
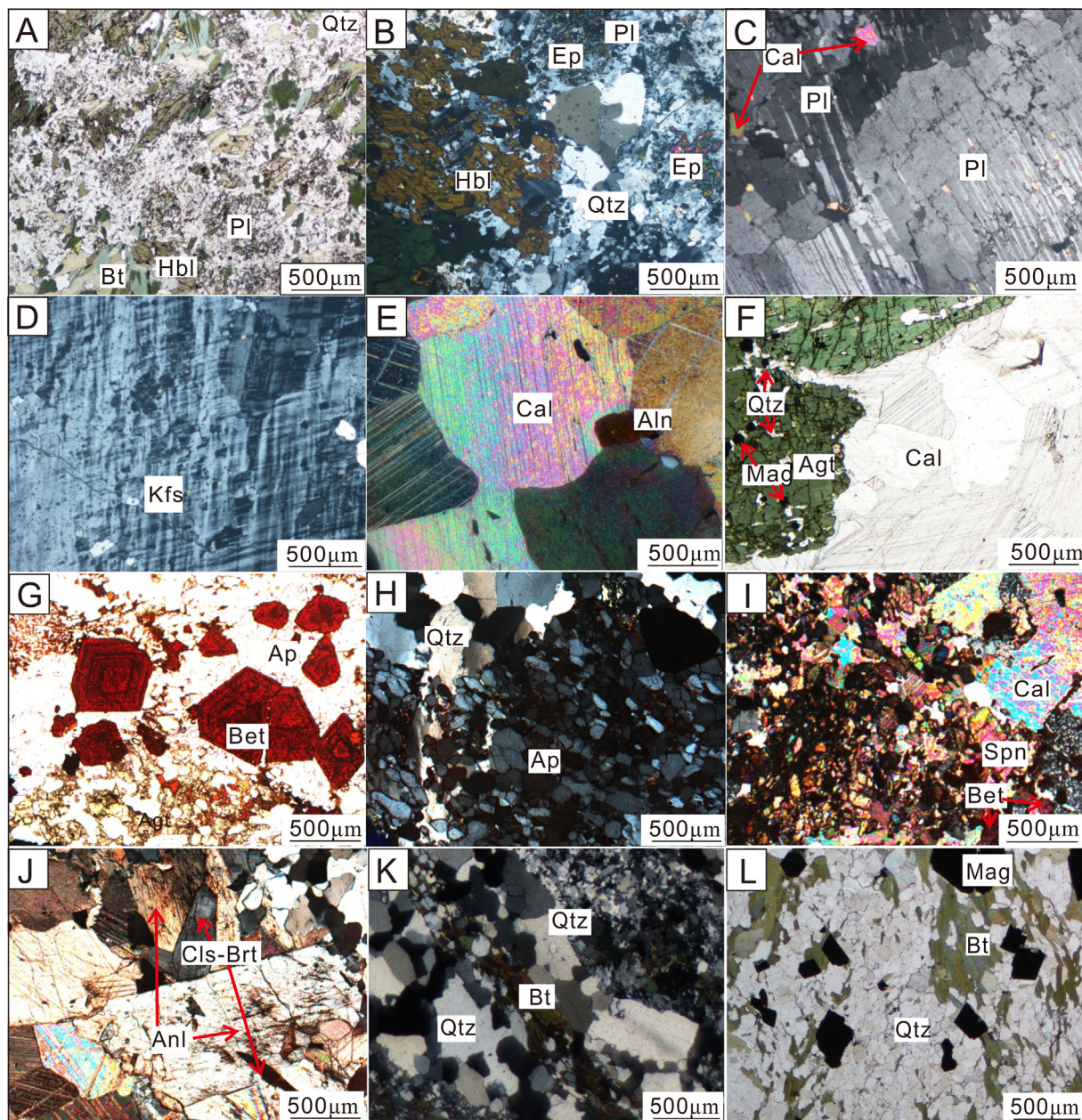
Fig. 3. Photomicrographs of the mineral assemblage in the drillhole. A and B: Taihua Group gneiss, including: quartz, plagioclase, biotite, amphibole and alteration mineral (epidote, chlorite and sericite); C and D: granite pegmatite, including: coarse quartz–biotite–K-feldspar–feldspar–allanite; E and F: Alkaline-riched carbonatite sub-stage, including: calcite and aegirine-augite (quartz and magnetite); G and H: Nb-U mineralization sub-stage, including: betafite, fluroapatite, calcite, aegirine-augite and sphene. I: REE-U enrichment sub-stage. J: Sulfate sub-stage, include celadite–barite–calcium–zeolite; K and L: Late reactivated mineralization stage, including: fine quartz, feldspar and biotite. Qtz: quartz; Pl: feldspar; Bt: biotite; Hbl: amphibole; Ep: epidote; Cal: calcite; Kfs: K-feldspar; Aln: allanite; Agt: aegirine-augite; Mag: magnetite; Bet: betafite; Ap: apatite; Spn: sphene; Cls-Brt: celadite–barite.

5.2. Drillhole alteration mineralogy

This study indicates that the U-Nb mineralizations were mainly related to carbonatite magmas and post-magmatic hydrothermal fluids. The main mineralization stage can be divided into four sub-stages according to distinctive mineral assemblage, including: alkaline-rich carbonatite sub-stage, Nb-U mineralization sub-stage, sulfate sub-stage, REE-U hydrothermal fluid sub-stage (Fig. 8). The alkaline-rich carbonatite sub-stage was accompanied by weak U-Nb mineralization. Plenty of calcite, aegirine-augite were crystallized at this early carbonatite stage (Fig. 3E and F). While only little pyrochlore grains occurred at this alkaline-rich sub-stage. The aegirine-augite has been latterly altered into sieve texture, which formed fine magnetite and quartz grains in the

aegirine-augite micro cavities. The calcite grains suffered no obvious alteration and still reserved their crystal morphology.

The Nb-U mineralization sub-stage is the most important stage to discuss in the mineralization process. In this sub-stage, mineral assemblages including betafite, fluroapatite, sphene, phlogopite with little calcite, aegirine-augite and allanite (Fig. 3G and H). Pyrochlore shows typical magmatic oscillatory zoning, most likely crystallized in the carbonatite magmas. Most betafites especially are accompanied with lager volume fluoroapatites. Remarkably, several tiny apatite inclusions are distributed among the grains of betafite, which may indicate that fluorine fugacity change to control the U-Nb mineralization.

The sulfate sub-stage could be indicated by evolution of sulphate-rich carbonatite magma having been affected by immiscible sulphate
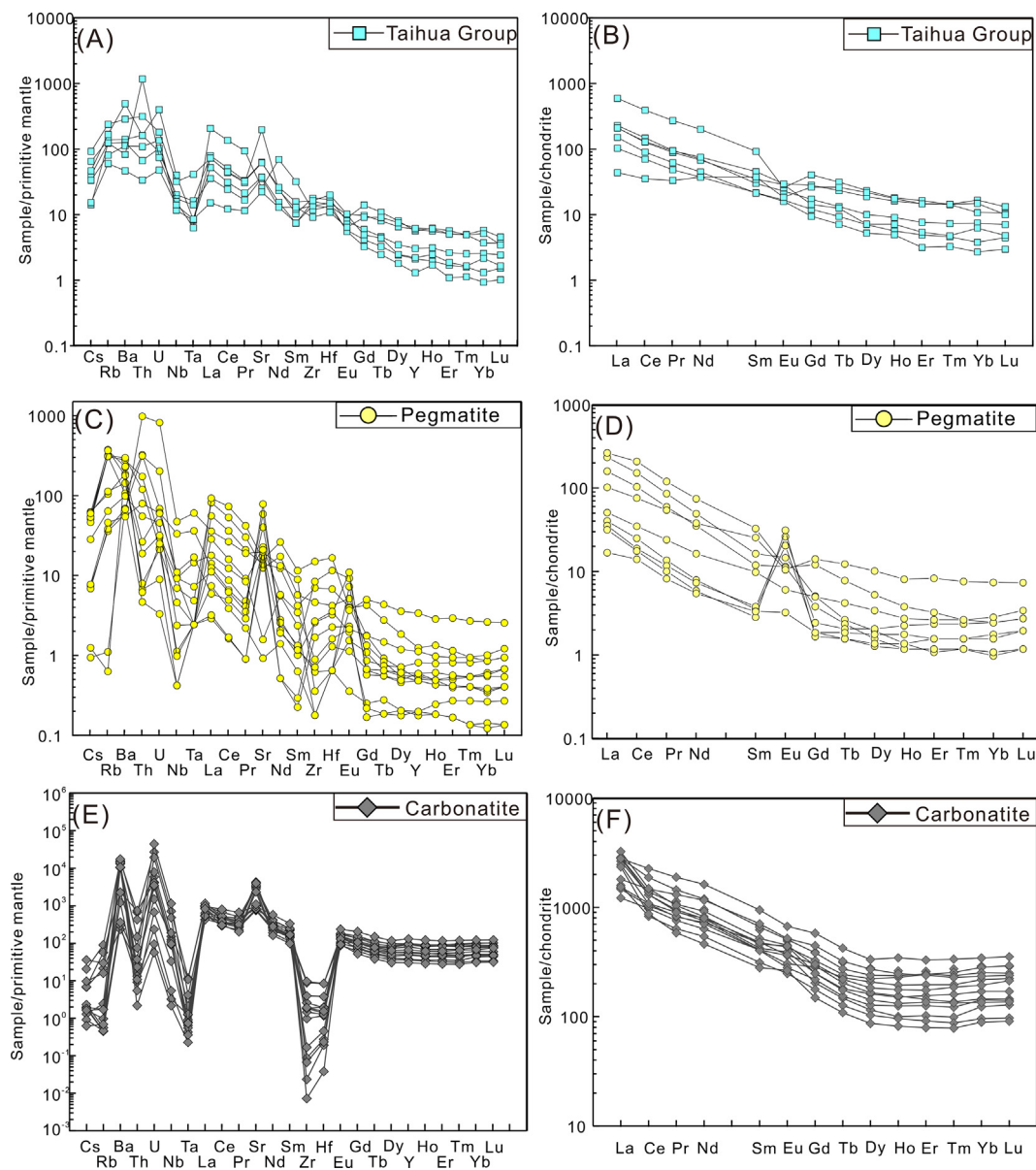
Fig. 4. Primitive-mantle-normalized trace element spider diagram and chondrite-normalized rare earth element (REE) pattern of Taihua Group gneiss (blue squares), pegmatite (yellow circles) and carbonatite dykes (grey diamond) from the drillhole. The chondrite values were obtained from (Sun and McDonough, 1989). (For interpretation of the references to colour in this figure legend, the reader is referred to the web version of this article.)

magma being present. Within certain temperature and pressure ranges, sulphate magma gets separated from carbonatite magma and forms the celadite-barite veins (Fig. 3I and J). The REE-U enrichment sub-stage could then have emerged during lower temperature magmatic hydrothermal stages. Yellow exannulate betafites accompanied with REE minerals (allanite and monazite) then would have appeared. After the main carbonatite U-Nb mineralization stage, fine-grained late quartz feldspar veins replaced and reactivated the early igneous carbonatite and U-Nb mineralization (Fig. 3K and L).

6. Discussion

6.1. Huayangchuan carbonatite petrogenesis

Mineral assemblages and geochemical evidences suggest that carbonatite dykes maintain a close relationship with U-Nb mineralizations. It is therefore crucial to clarify the source and petrogenesis of Huayangchuan carbonatite. Carbonatite rocks have gone through at

least one of the processes as follows, including: 1) directly partial melting from carbonated peridotite or eclogite (Chakhmouradian, 2006; Harmer and Gittins, 1998; Sweeney, 1994; Dasgupta and Hirschmann, 2006; Thomson et al., 2016); 2) immiscible differentiation from carbon-rich alkaline silicate magma (Halama et al., 2005; Ivanov et al., 2010; Thomsen and Schmidt; 2008); 3) derivation of CO_2-rich silicate magmas from crystal fractionation (Tappe et al., 2012; Veksler et al., 1998). While it is hard to interpret what causes high levels of CaO from a simple melting model, low amounts of MgO and of alkali contents in carbonatites from Huayangchuan, as well as Bayan Obo and Taohuala Mountain (Fan et al., 2016; Ling et al., 2013; Mitchell, 2005; Yang et al., 2009; Xue et al., 2018a). Carbonatite melt generated from mantle peridotite and eclogite source should have composition (high MgO contents) well balanced with mantle peridotite. Primary carbonatite melt should contain relative high alkali contents (Na_2O + K_2O), due to high alkali elements dissolution capacities.

Subsequent differential processes are required, in order to evolve primary carbonatite melts into presenting higher CaO content and
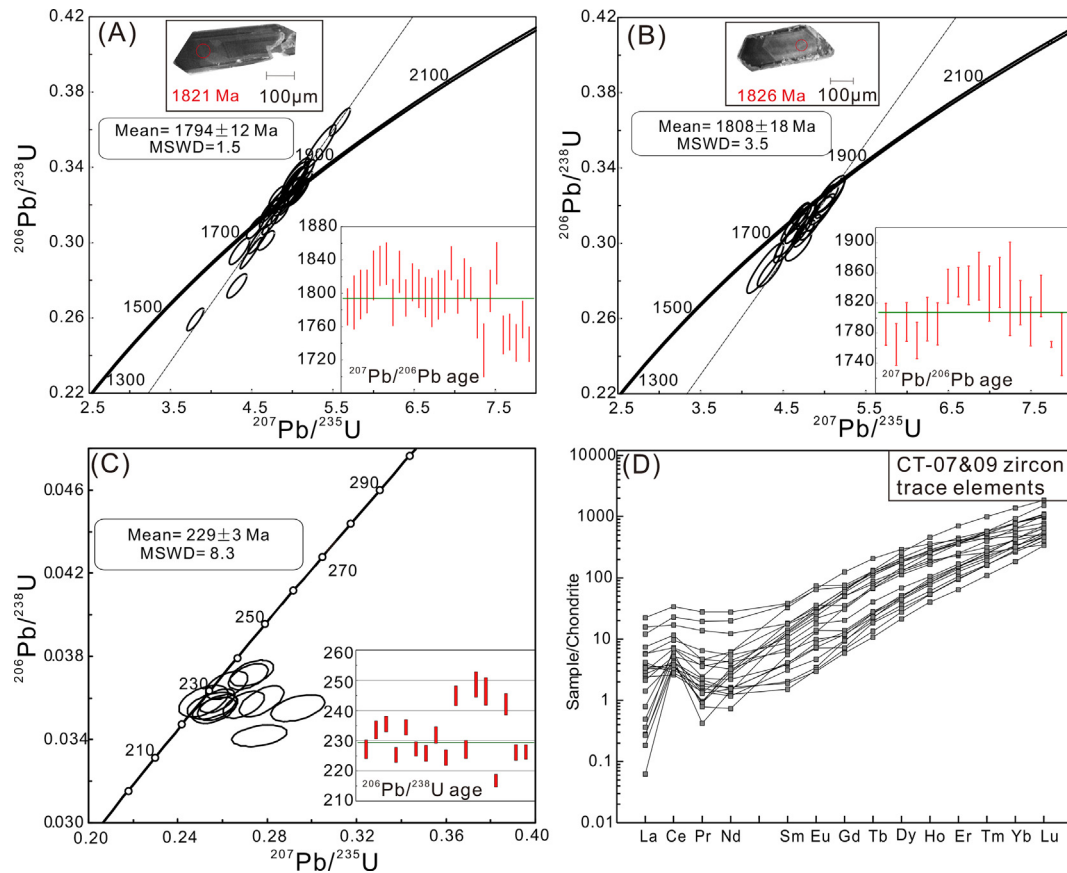
Fig. 5. A and B: Zircon concordia diagrams of granite pegmatite rocks from the Huayangchuan district. C: Zircon concordia diagrams of carbonatite rocks from the Huayangchuan district. D: Chondrite-normalized rare earth element (REE) pattern for zircons from carbonatite rocks of the Huayangchuan district. Chondrite normalization values are from Sun and McDonough (1989).

lower MgO, SiO$_2$ and alkali contents. The liquid immiscible process between alkali silicate melt and evolved carbonatite melt can appear at 1 ~ 3 GPa with 1150 ~ 1260 °C (Martin et al., 2013; Dasgupta et al., 2006). This differential process can cause high CaO (up to 30 wt%), high Ca/(Ca + Mg + Fe) (up to 0.85) and low SiO$_2$ while putting carbonatite melt in segregation. In anhydrous system, carbonatite melt displays higher Na$_2$O + K$_2$O relative to silicate melt. While in H$_2$O-bearing system, there are no big differences in alkali contents between two kinds of melts. Crystallization differentiation of olivine, clinopyroxene, calcite and other accessory minerals (perovskite, betafite, apatite) could lower SiO$_2$, MgO, K$_2$O + Na$_2$O and increase CaO in residual magma, which also can transfer primary magnesio-carbonatite to calcio-carbonatite.

As for liquid immiscible differentiation process, the element (i) concentration in carbonatite melt by the element (i) concentration in primary melt can be shown in the following equation:

$$C_{CL}/C_O = (F/D_i + 1 - F)^{-1}$$

C_{CL} is the concentration of element (i) in differential carbonatite melt, C_O is the element (i) concentration in primary melt prior to liquid immiscible process, F is the proportion of silicate melt and D_i is the partition coefficient between carbonatite and silicate melts. For example, if we assume that F is equal to 10%, which means 10% silicate melt and 90% carbonatite melt, such as generated during the liquid immiscible process. From the expression, D_i values determine the enrichments or depletions of element (i) that take place in carbonatite melt. If $D_i > 1$, the carbonatite melt will enrich element (i) relative to primary melt. Otherwise, if $D_i < 1$, the carbonatite melt will be depleted in the element (i) relative to primary melt. According to D_i values from Martin et al., (2013), Hamilton et al. (1989), Jones et al.

(1995), and Veksler et al. (1998, 2012), we can draw a conclusion that immiscible differentiation can induce Ba and Sr enrichments, HFSE depletions and change in REE amounts, whether enrichment or depletion depending on varied D_{REE} (from 0.1 to 7). Such enrichments and depletions are relative slight due to given D_i values (near 1). According to D_{La}/D_{Lu} in a range from 1.6 to 2.3, liquid immiscible process could only form slight LREE and HREE differentiation in carbonatite melt in comparison with primary melt.

The crystallization differentiation process can obviously modify the residual carbonatite melt composition. Olivine and clinopyroxene crystallization can decrease SiO$_2$, MgO and Na$_2$O contents as well as increasing LILE (Ba, Sr, Th, U and LREE) concentrations (Dasgupta et al., 2006; Blundy and Dalton, 2000; Klemme et al., 1995). Calcite crystallizations can enrich these LILE and HFSE in residual magma, while almost have slight influence in varying REE concentrations because $D_{Calcite/Carbonatite}$ of REE are almost near 1 (Xue et al., unpublished materials). Simple crystallization differentiation of olivine, Clinopyroxene, calcite cannot explain the depletion of Nb, Ta, Zr, Hf and high Nb/Ta ratios. Accessory minerals (e.g., perovskite) can strongly decrease HFSE concentration and increase the Nb/Ta ratios due to high partition coefficient (Xue et al., unpublished materials).

6.2. Shallow upper lithospheric mantle source with sediments assimilation

Although liquid immiscibility and crystallization differentiation can promote primary high alkali and MgO carbonatite evolution. These two differential processes can also enhance U, Ba, Sr and REE enrichments in residual carbonatite melt, benefitting for Huayangchuan U-Nb mineralization. The above differentiation and evolution processes could more or less promote LREE and HREE differentiation, which means the
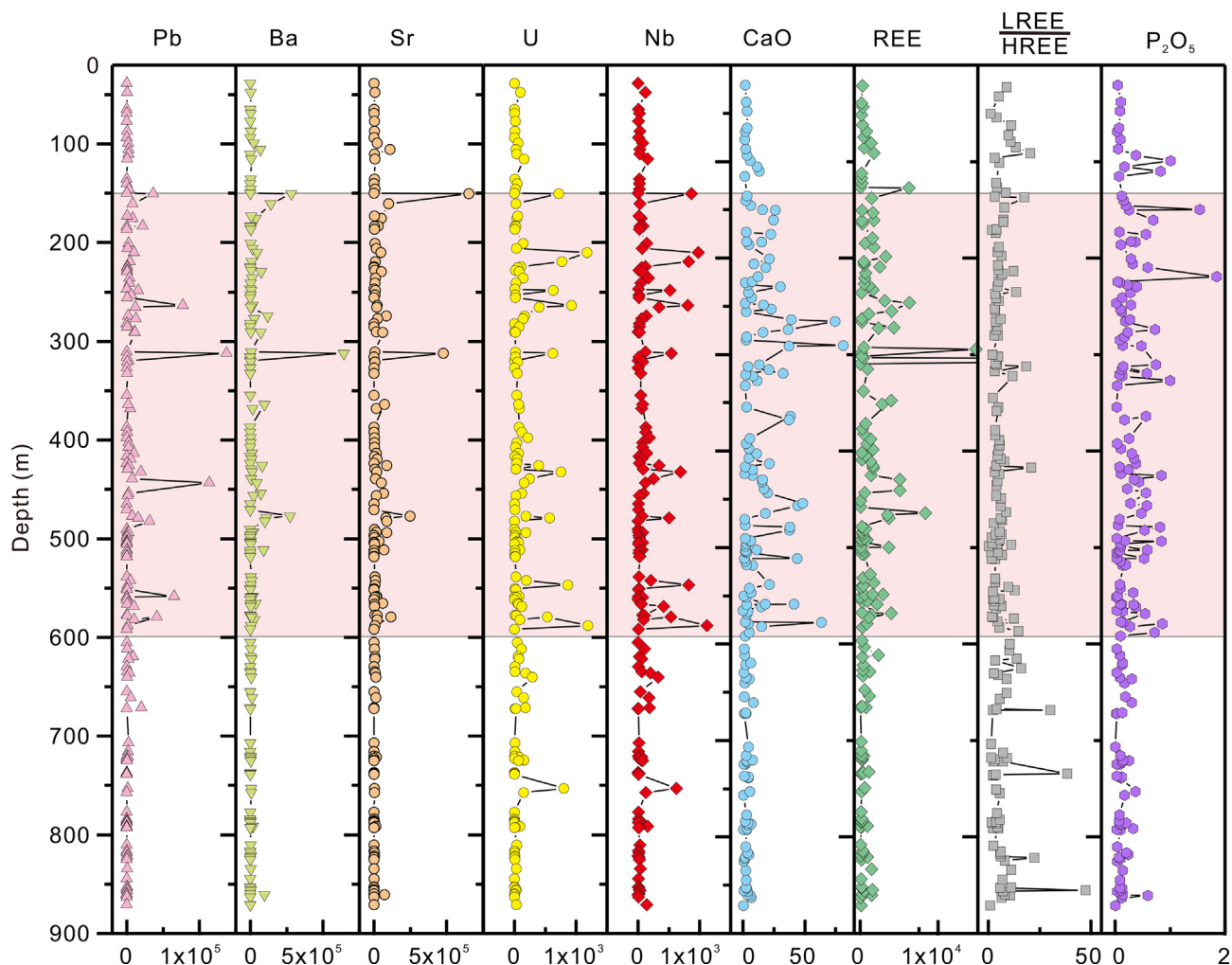
Fig. 6. The diagram between depth and major and trace elements, such as: CaO, P₂O₅, U, Nb, Pb, REE, LREE/HREE, Sr, Ba. The yellow area indicates large volume carbonatite dykes intruded into the wall rock (Taihua Group and granite pegmatite). U-Nb-REE mineralization mainly occurred in the carbonatite dykes. (For interpretation of the references to colour in this figure legend, the reader is referred to the web version of this article.)
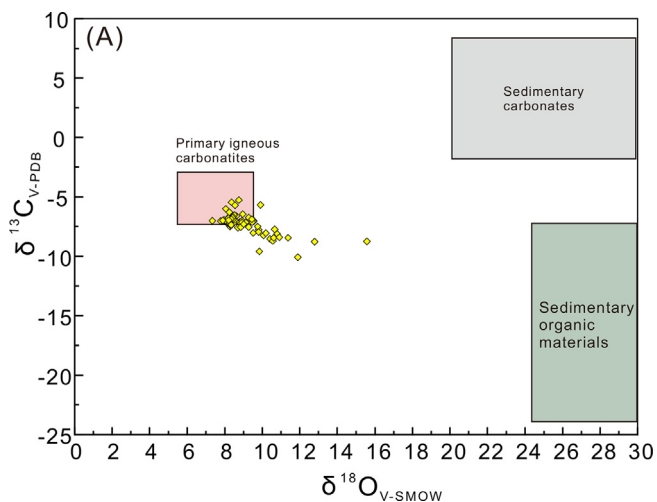

Fig. 7. C-O isotopic composition of the Huayangchuan carbonatite (date from this study) and global carbonatites (Table A5). Most samples show the contribution of mantle to the carbonatite source. Mantle and marine sediment boxes for carbonatites from Taylor et al. (1967) and Keller and Hoefs (1995).

lateral stage carbonatite should have high LREE/HREE and La/Yb ratios than primary melts. While the outcropped carbonatite dykes in Huayangchuan district all show slight LREE enrichments and low La/Yb ratios. Regardless which mechanisms, the primary Huayangchuan carbonatite melt should present the same or an even flatter REE distribution pattern, but occurring only very rare in all carbonatite worldwide.

It is commonly supposed that carbonatite melts basically formed deep in the mantle, which melt from carbonated garnet peridotite or eclogite. Considering the distribution coefficients between mantle minerals (olivine, clinopyroxene, orthopyroxene and garnet) and carbonatite melt, the proportion of garnet mainly control the differentiation of LREE and HREE. The proportion of garnet in mantle peridotite increase with increase of depth and pressure. The shallow mantle should have either less or no garnet than deep mantle. It is more reasonable for Huayangchuan carbonatite melts to generate from shallow upper lithospheric mantle (< 3 GPa or < 100 km).

The Huayangchuan carbonatite is characterized by extreme enriched Sr-Nd-Pb [(^{87}Sr/^{86}Sr)$_i$ = 0.7048–0.7057; ε_{Nd} = −4.3 to −10.1; ^{207}Pb/^{206}Pb = 0.878–0.889] isotopic features compared to typical carbonatites globally (e.g., East African, North America, Brazil carbonatites). Previous literatures suggested that most of the world's carbonatites derive from carbonated lithospheric mantle, and are triggered by either asthenospheric upwelling or plume activity (Bell and Simonetti, 2010). However, this model cannot explain the high Ba, U and enriched Sr-Nd isotopic arrays for the Huayangchuan carbonatite
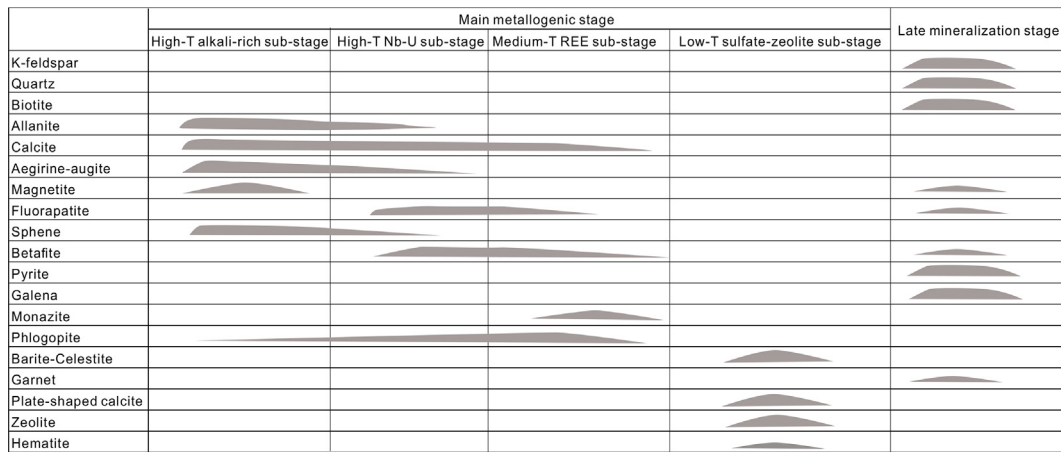
	Main metallogenic stage				Late mineralization stage
	High-T alkali-rich sub-stage	High-T Nb-U sub-stage	Medium-T REE sub-stage	Low-T sulfate-zeolite sub-stage	
K-feldspar					▭
Quartz					▭
Biotite					▭
Allanite	▭	▭			
Calcite	▭	▭	▭		
Aegirine-augite	▭	▭			
Magnetite	▭				▭
Fluorapatite		▭	▭		▭
Sphene	▭	▭			
Betafite					▭
Pyrite					▭
Galena					▭
Monazite			▭		
Phlogopite					
Barite-Celestite				▭	
Garnet					▭
Plate-shaped calcite				▭	
Zeolite				▭	
Hematite				▭	

Fig. 8. Minerals assemblage generation analysis of typical drillhole samples in the Huayangchuan ore district.

(Fig. 9 a, b, c and d). Recently, many researchers have paid attention to the genetic relationship between carbonatite and recycled sedimentary carbonates in subduction process (Barker, 1996; Bell and Simonetti, 2010; Chen et al., 2016; Halama et al., 2008; Hou et al., 2006, 2015; Liu et al., 2015; Song et al., 2016; Woodard and Huhma, 2015; Xu et al., 2015, 2018a). However, how the recycling sediments contribute to the carbonatite magmas in subduction zone is still unclear. Some researchers suggested that melting of carbonate-bearing oceanic slab may generate the relative enriched Sr-Nd-Pb and low Mg ($\delta^{26}Mg = -1.89 \sim -1.07‰$) isotopic features (Song et al., 2016; Xu et al., 2011). Although the melting of carbonated oceanic eclogite could generate the similar isotopic characteristics, the type of model thereof in question fails to explain the high CaO content, relative flat REE distribution model and the highly varied range of Nb/Ta ratios.

Subducted carbonate sediments recycling can be subdivided into three cycles: (1) detached sedimentary carbonates from oceanic slab enter the mantle at ~80–100 km due to their low density and high rheology. (2) calcio-carbonatitic fluid is formed by the Ca-rich carbonates dissolutions during the slab dehydration process at the depth of 120–200 km; (3) deep cycle, magnesio-carbonatite melt is generated by the Mg-rich carbonates melting from the carbonated ocean eclogite at 300 ~ 650 km (Li et al., 2017). The flat REE characteristics of Huayangchuan carbonatite suggest that detached recycled marine sediments are more likely involved in the upper lithospheric mantle and provide the main source for carbonatite magma.
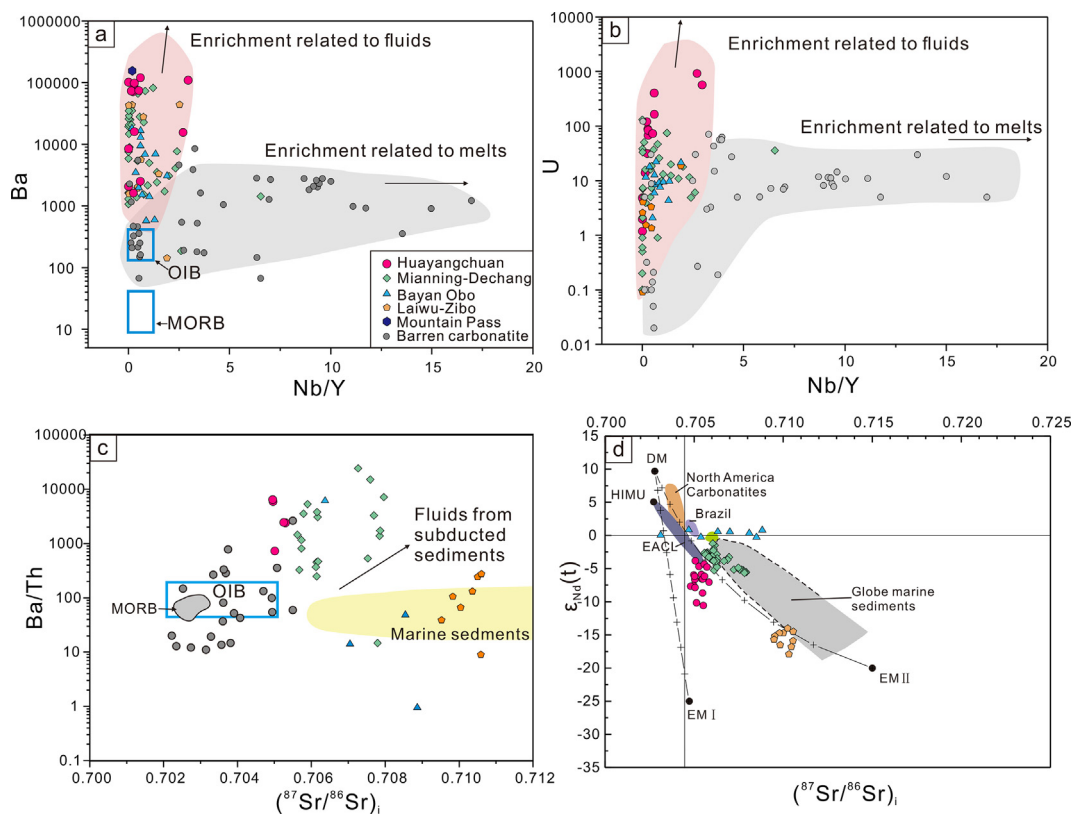
Fig. 9. Plots of (A) Ba vs. Nb/Y, (B) U vs. Nb/Y, (C) Ba/Th vs. $^{87}Sr/^{86}Sr$ and (D) $\varepsilon_{Nd}(t)$ vs. $(^{87}Sr/^{86}Sr)_i$ for the Huayangchuan carbonatites and most global carbonatites. Data are from the Supplementary Tables A2–5.

6.3. Source assimilation of Huayangchuan carbonatite by organic sediments

Carbon and oxygen isotope composition of the calcite in the Huayangchuan carbonatite is mostly consistent with its mantle origin, falling within the range of primary carbonatites (-8 to -4% and 6 to 10%) (Taylor et al., 1967). However, there still are several carbon and oxygen isotope composition of calcite plots outside the mantle field, such that reveal a wide range of variations. Specially, the C-O isotopic values of unaltered samples show relative variation trend, such that $\delta^{13}C$ values decrease during increase in $\delta^{18}O$ values. Several factors could result in such varied C-O isotope shifts in carbonatite magmatism and post-magma hydrothermal stage. These mainly include magmatism evolution, contamination by country rocks, magma degassing process, and source assimilation (Demény et al., 2004; Demeny et al., 1998).

Above all, studies of magmatic evolution have shown that fractional crystallization and liquid immiscibility may not significantly affect the oxygen and carbon isotopic composition of carbonatites (Kalamarides, 1984). Though high temperature crystallization of calcite could induce the C-O isotopic shifts in the carbonatite (Trofanenko et al., 2016). While this crystallization process could only result in the positive $\delta^{13}C$ and $\delta^{18}O$ shifts. Besides, country rock contamination is an important mechanism, which will likely modify the oxygen isotope composition of carbonatite. However, except for the samples contaminated by limestone from the country rock, there are no large carbon isotope differences among the samples. The Taihua gneiss is the wall-rock of Huayangchuan carbonatite dykes. Even contamination of high proportions of gneiss could not cause such high changes in C isotopic characteristics.

In addition, some researchers have supposed that varying degrees of degassing of CO_2 might have been responsible for the C-O isotopic variations we have observed. CO_2 released from carbonatitic magma is enriched in ^{13}C relative to the residual C dissolved in the magma (Javoy et al., 1978; Mattey, 1991). As reported by Pineau and Javoy (1983), CO_2 degassing can lead to very negative $\delta^{13}C$ values in basaltic rocks (down to -20.6). The degassing of volatiles (including CO_2 and H_2O) mainly control the negative $\delta^{13}C$ shift (Demeny and Harangi, 1996). At the same time, degassing of CO_2 couldn't induce such a C-O isotopic negative correlation trend, in which C isotopic values decrease with an increase in O isotopes. According to our numerical modeling of degassing process (Fig. 10), the samples that reveal distinct features with CO_2 degassing process.

The mantle source assimilated by organic sediments should be the more reasonable way to explain C-O isotopic characteristics. A two end member mixing model can interpret C isotope negative shift as well
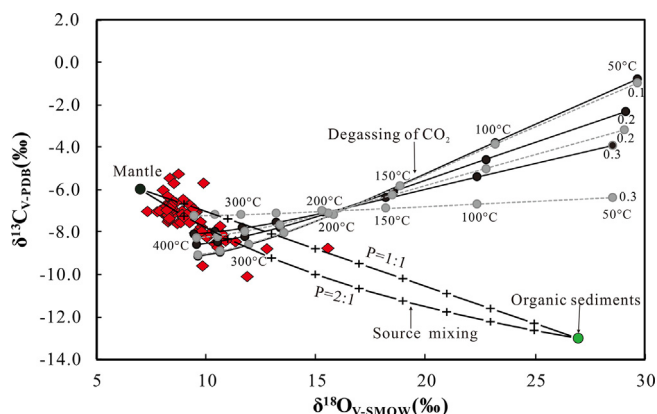

Fig. 10. C-O isotope variations by simulated CO_2 degassing and organic materials mixing. The batch (solid lines) and Rayleigh (dashed lines) degassing-precipitation models change progressively the temperatures and mol fractions of carbon in the degassed CO_2 (shown by the numbers near the lines) (after Zheng, 1990). The $\delta^{13}C$ and $\delta^{18}O$ values of the initial carbonatite were taken as -6‰ and 7‰, respectively.

as O isotope positive shift (Fig. 10). It is widely accepted that organic materials could subducted into mantle and alter the mantle C-O isotopic composition. Available studies suggest the possibility that OIBs have C isotopes that are lighter than MORB, suggesting organic C materials contribution (Gerlach et al., 2002; Exley et al., 1986; Aubaud et al., 2006; Eguchi and Dasgupta, 2017). The organic-rich sediments generally are enriched with U and Mo due to low redox state, inferring that such sediments may be the source of ore-forming materials.

6.4. Uranium-niobium transportation and precipitation mechanism

The Nb and U are mainly endowed within betafite in the Huayangchuan deposit. Precipitation of pyrochlore in carbonatite can only occur according to particular conditions. Mitchell and Kjarsgaard (2004) suggested that F-rich magma is critical in stabilizing pyrochlore-group minerals in carbonatites by high T-P experiments. High F concentration also can explain the high Nb/Ta ratios. Wang et al. (1982) showed that Nb and Ta fluorine complexes have different thermal stabilities where Ta-fluorine complexes are more mobile and stable at lower temperature than Nb-bearing complexes, therefore, the tendency for Nb to crystallize from the melt in early stages. In the drillhole samples, apatite becomes a very important fluorine mineral. Apatite from the Huayangchuan carbonatite has high F (3.1–4 wt%) and low Cl concentrations (0.004–0.012 wt%). This study also suggests that the apatite had been formed in an environment of high fluorine fugacity (Brenan, 1993).

Contemporaneous carbonatite magmatic composition can be revealed by observing apatite trace element composition. The high Sr concentration (~5200 ppm) in apatite (ZK2003-53) is consistent with other apatite in carbonatite globally (Belousova et al., 2002). The average Nb and U concentrations in apatite are 0.47 ppm and 8.18 ppm, respectively. The Nb and U concentrations of carbonatite magmas or fluids should be 118 and 8000 ppm according to the partition coefficient (D) between apatite and carbonatite melts (Klemme and Dalpe, 2003). The mineralized carbonatite apatite was compared with unmineralized carbonatite apatite in Huayangchuan (i.e., Caotan carbonatite). From the Sr-F, U-F, Nb-F diagrams, the two kind of apatites have clear difference trace element characteristics, such as Sr, U, Nb, REE and so on (Fig. 11 a, b, c and d). In general, the high-F apatite also has relative high concentration of U and Nb, which reflect the high U-Nb contents carbonatite magmas. U-Nb mineralization have intimate relationship with the high-F carbonatite magmas. The fluorine contents in the carbonatite magmas potentially could have accelerated Nb solubility (Kjarsgaard and Mitchell, 2008). We can infer that the Huayangchuan carbonatite partial melting from the mantle contained high F concentration and high Nb and U ore-forming materials from the mantle source.

In the carbonatite magma, Nb and Ti are soluble as, e.g., carbonate, fluorine, phosphate complexes (Aleksandrov, 1967; Aleksandrov et al., 1985). Uranium is soluble as fluorine and sulphate complexes under acid conditions, such as phosphate complexes under neutral conditions and such as carbonate and hydroxide complexes are under alkaline conditions (Boyle, 1980). Because the concentrations of the complex ligands such as phosphate, fluorine and carbonate are high in the carbonatite magma, the U and Ti are likely to be soluble and hence not precipitated in the early high alkali carbonatite stage. That is also consistent with what we know from the Huayangchuan deposit. As the concentrations of phosphate, fluorine and carbonatite decrease, what Ti and U are kept in late post-magmatic hydrothermal stage will be precipitated. Therefore, the decrease of carbonate, fluorine, phosphate complexes is really important to the transportation and precipitation of U, Nb and Ti.

Dropping in concentration of the complex anions will occur: (1) shallow level degassing; (2) precipitation of F-bearing minerals; (3) interaction with wall rock (Knudsen, 1989). Firstly, extensive crystallization of F-free minerals (e.g., calcite, aegirine-augite) results in
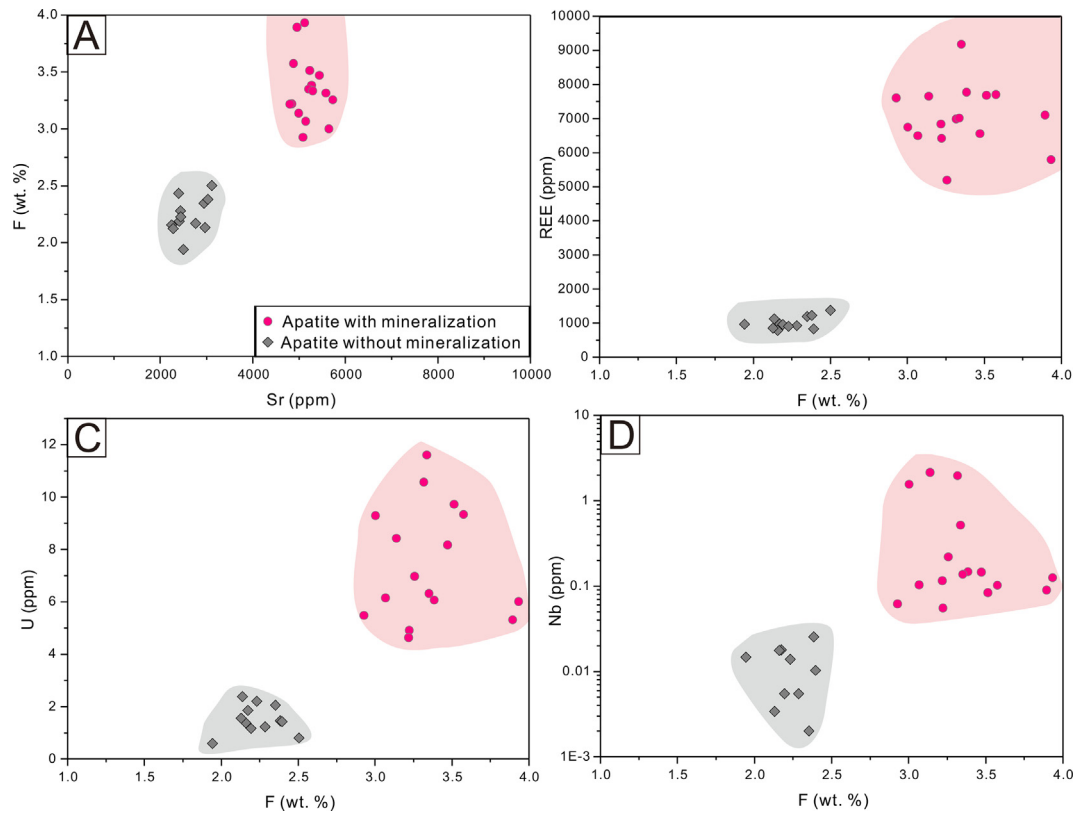
Fig. 11. The trace element difference between mineralized apatite and unmineralized apatite in the Huayangchuan ore deposit. A: Sr versus F (wt. %) diagram; B: F (wt. %) versus REE diagram; C: U versus F (wt. %) diagram; D: Nb versus F (wt. %) diagram.
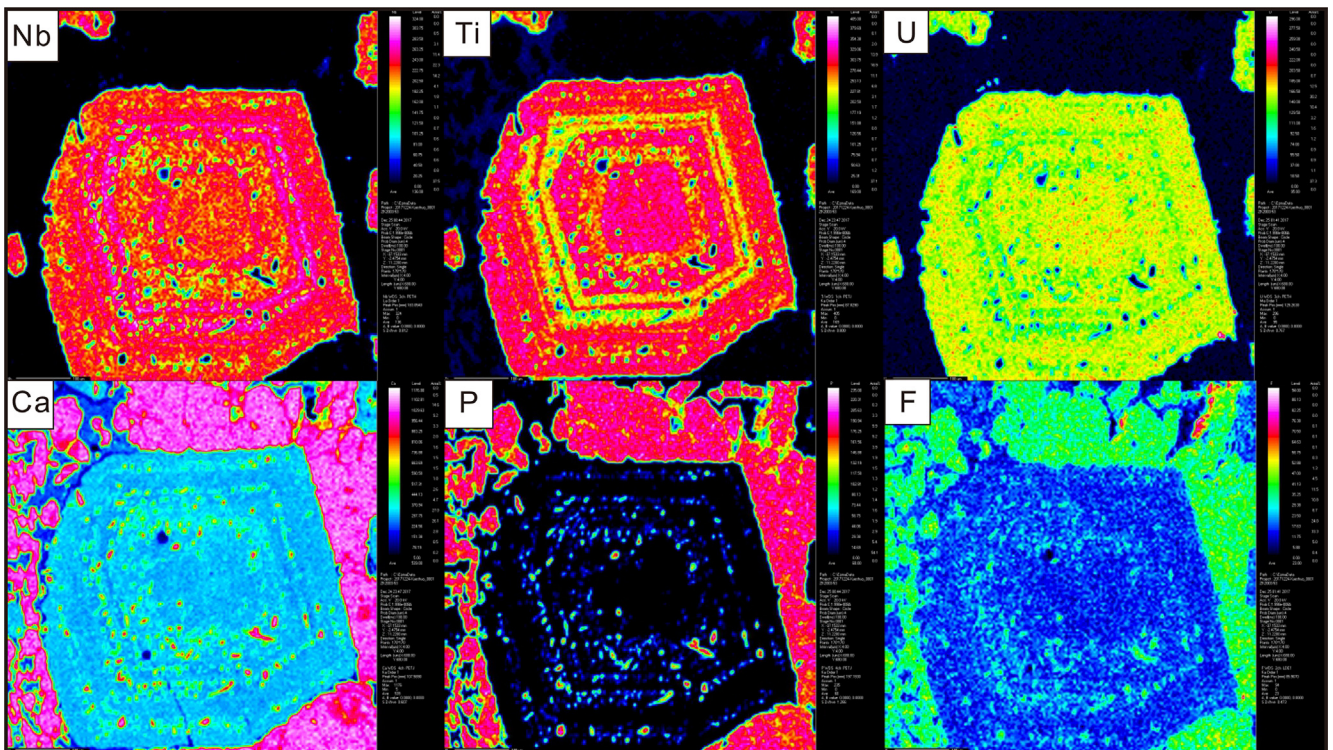

Fig. 12. Major element intensity mapping of betafite with oscillatory zone by EPMA.
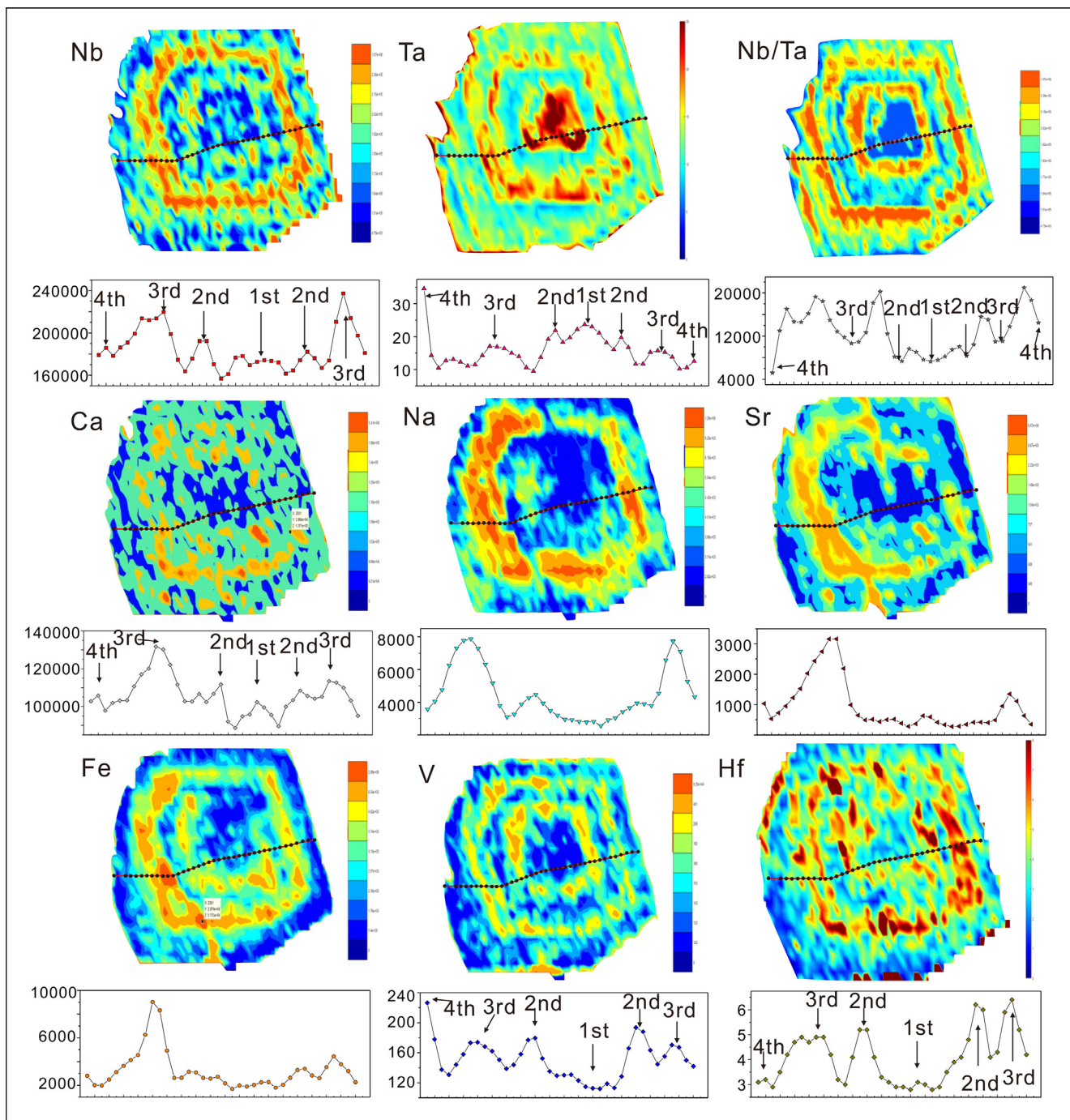
Fig. 13. Trace element mapping of betafite with oscillatory zone by LA-ICP-MS. Four stages (1st, 2nd, 3rd, 4th) could be distinguished by chemical composition differences.

increasing F contents in the residual melt. When reaching its solubility limit, excess F would escape from the melt by degassing. The negative $\delta^{13}C$ and $\delta^{18}O$ shifts suggest that volatiles (CO_2) degassing process is negligible during the carbonatite evolution. Secondly, the F concentrations are mainly governed by the crystallization of F-bearing minerals (mainly by fluorapatite). Crystallization of halogen-bearing minerals (e.g., apatite and titanite) could (at least partly) decrease the F concentration in the residual magmas or fluids. In fact, that betafite in Huayangchuan is found at the carbonatite-wall rock boundary. The positions of betafite crystallization are generally accompanied with large amounts of fluroapatite, indicates that the decrease of complex ligands concentration actually was responsible for the precipitation of betafite.

Fine crystalline zonings could be clearly found in betafite, reflecting the crystal growing process. Major and trace element mapping analysis were performed in the euhedral betafite with fine oscillator zoning. As the Figs. 12 and 13 shown, four stages primary oscillator zonation in one betafite grain could be distinguished by chemical differences. From core to rim, Nb, U, Ca, Ti, P and F also display oscillatory zoning features, similar to other carbonatite pyrochlore globally (Knudsen, 1989). In the betafite grain, tiny apatite inclusions could be found and trapped among the oscillatory zoning. Combining with the large volume apatite grains grew around betafite, these evidences together indicate that betafite precipitated simultaneously with apatite. Several trace
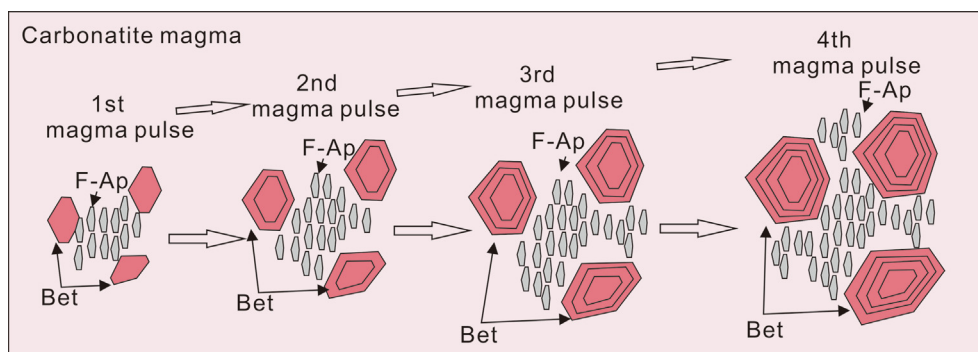
Fig. 14. Diagram of precipitation of betafite with fluorapatite. A: Taihua Group gneiss intruded by carbonatite dykes; B: Precipitation of betafite with fluorapatite. This diagram is consistent with major and trace element compositions shown in Figs. 12 and 13.
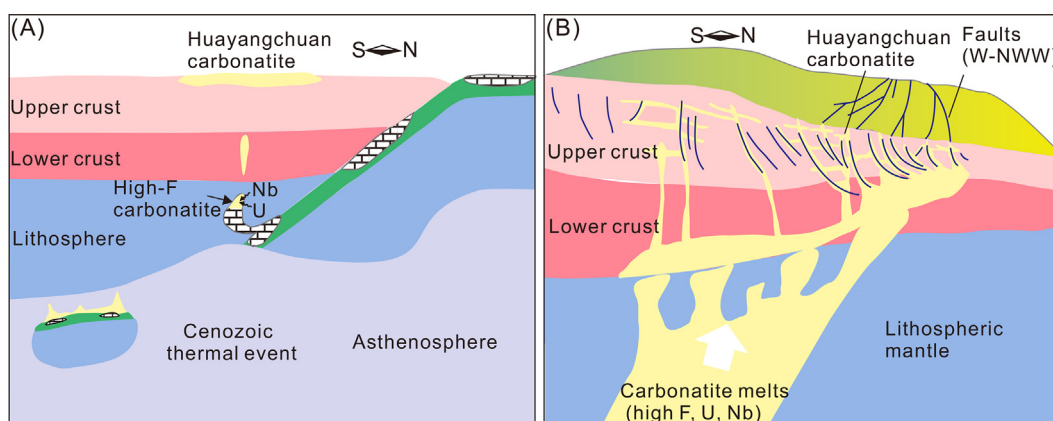

Fig. 15. The Huayangchuan giant U-Nb ore deposit and carbonatite genesis schematic diagram. A: Lithospheric mantle metasomatized by sedimentary carbonates during slab subduction; B: Carbonatite magmas generated from the carbonated mantle during post-orogenic tension stage.

elements (such as Fe, Ta, Hf, Na, V) display similar varieties from core to rim. Fe, Hf, V, Na show obvious affinity with Nb and Ca. The betafite have high Sr concentrations (range from 275 to 2188 ppm), which are balanced with high Sr carbonatite magmas. The high Sr concentrations of betafite also prove the carbonatite type U-Nb mineralization rather than the other type mineralization. The oscillatory zones of betafite is interpreted as the result of continuous precipitation of betafite with a composition in equilibrium with a fluid with increasing concentration of the complex ligands, during the intrusion of carbonatite (Fig. 14).

6.5. An integrated genetic model for the Huayangchuan deposit

Huayangchuan carbonatite dykes intruded into the Taihua gneiss at ~230 Ma, roughly at the post-collision stage of the Mianlue Ocean closure. Subduction of the Mianlue Oceanic slab or earlier oceanic slab has been regarded to carry large volume of carbonate sediments into mantle peridotite. This recycling of subducted marine sediments also contain plenty of ore-forming materials (U, Nb and REE) into mantle (Meng and Zhang, 2000; Sun et al., 2002). Similar mantle enrichment by subducted sediments has also been recognized in the Mianning-Dechang, Bayan Obo and Taohuala Mountain districts (Hou et al., 2015; Ling et al., 2013; Xue et al., 2018a). The Huayangchuan high F carbonatite magma were generated by melting of fertilized carbonated mantle during subduction process, resulting in that magmas had ascended along trans-lithospheric faults along craton edges, emplaced within shallow crust (Fig. 15).

Subsequently, high-F carbonatite magma with abundant ore-forming materials (Nb, U and Pb) intruded into the Taihua Group gneiss and pegmatite in the Huayangchuan district. Nb, U and Ti was preferentially incorporated in the late stage carbonatite magmas or hydrothermal fluids rather than precipitated in the early highly alkali carbonatite stage. Niobium, U and Ti are soluble as carbonate, phosphate, fluorine and sulphate complexes. Precipitation of apatite and wall rock interaction commonly result in the complex ligands decrease and precipitation of betafite. That explains the common betafite-fluorapatite association in carbonatites worldwide.

7. Conclusions

The Huayangchuan U-Nb deposit is a giant deposit related with carbonatite magmatism, as located in the Lesser Qinling district. The Sr–Nd–C–O isotopic compositions and trace element patterns suggest the Huayangchuan carbonatite was formed by partial melting of lithospheric mantle enriched by subducted carbonate sediments. Zircon U-Pb dating of the Huayangchuan carbonatite yielded Triassic ages of 229 ± 3 Ma, perhaps implying that mantle peridotite was metasomatized by sedimentary carbonates during the post-collision stage of Mianlue ocean subduction. Simple direct melting of carbonated peridotite alone can't induce Nb, U and Pb mineralization. The immiscibility and crystallization processes are then crucial to explain the high CaO content and the enrichment of LILE (Sr, Ba and U) in carbonatite. Relative flat REE pattern has thereby indicated at what depth melting had occurred in the shallow mantle (< 3 GPa, 100 km). A decrease of fluorine fugacity in later carbonatitic magmatism due to fluorapatite crystallization eventually resulted in betafite mineralization.

Declaration of Competing Interest

The authors declare that they have no known competing financial interests or personal relationships that could have appeared to influence the work reported in this paper.

Acknowledgements

Appendix A. Supplementary data

Supplementary data to this article can be found online at https://doi.org/10.1016/j.oregeorev.2020.103498.

References

Aleksandrov, I., 1967. Niobium in the carbonate solutions and some considerations on the migration of rare elements under hydrothermal conditions. Geochem. Int. 4, 558–566.

Aleksandrov, I., Krasov, A., Kochnova, L., 1985. The effects of potassium, sodium and fluorine on rock-forming mineral assemblages and the formation of tantaloniobate mineralization in rare-element granite pegmatites. Geochem. Int. 22, 85–94.

Aubaud, C., Pineau, F., Hékinian, R., Javoy, M., 2006. Carbon and hydrogen isotope constraints on degassing of CO_2 and H_2O in submarine lavas from the Pitcairn hotspot (South Pacific). Geophys. Res. Lett. 33 (2).

Barker, D.S., 1996. Consequences of recycled carbon in carbonatites. Can. Mineral. 34, 373–387.

Bell, K., Simonetti, A., 2010. Source of parental melts to carbonatites–critical isotopic constraints. Mineral. Petrol. 98, 77–89.

Belousova, E.A., Griffin, W.L., O'Reilly, S.Y., Fisher, N.I., 2002. Apatite as an indicator mineral for mineral exploration: trace-element compositions and their relationship to host rock type. J. Geochem. Explor. 76, 45–69.

Blundy, J.D., Dalton, J., 2000. Experimental comparison of trace element partitioning between clinopyroxene and melt in carbonate and silicate systems, and implications for mantle metasomatism. Contrib. Mineral. Petrol. 139, 356–371.

Boyle, R.W., 1980. Geochemical prospecting for uranium and thorium deposits. At. Energy Rev. 18, 3–72.

Brenan, J.M., 1993. Partitioning of fluorine and chlorine between apatite and aqueous fluids at high pressure and temperature: implications for the F and Cl content of high P-T fluids. Earth Planet. Sci. Lett. 117 (1–2), 251–263.

Cao, J., Ye, H.S., Li, H.Y., Li, Z.Y., Zhang, X.K., He, W., Li, C., 2014. Geological characteristics and molybdenite Re-Os isotopic dating of Huangshuian carbonatite vein-type Mo (Pb) deposit in Songxian County, Henan Province. Mineral Deposits 33 (1), 53–69.

Chakhmouradian, A.R., 2006. High-field-strength elements in carbonatitic rocks: geochemistry, crystal chemistry and significance for constraining the sources of carbonatites. Chem. Geol. 235, 138–160.

Chakhmouradian, A.R., Zaitsev, A.N., 2012. Rare earth mineralization in igneous rocks: sources and processes. Elements 8 (5), 347–353.

Chen, C., Liu, Y., Foley, S.F., Ducea, M.N., He, D., Hu, Z., Chen, W., Zong, K., 2016. Paleo-Asian oceanic slab under the North China craton revealed by carbonatites derived from subducted limestones. Geology 44, 1039–1042.

Dahlkamp, F.J., 1978. Classification of uranium deposits. Miner. Deposita 13, 83–104.

Dasgupta, R., Hirschmann, M.M., 2006. Melting in the Earth's deep upper mantle caused by carbon dioxide. Nature 440, 659–662.

Dasgupta, R., Hirschmann, M.M., Stalker, K., 2006. Immiscible transition from carbonate-rich to silicate-rich melts in the 3 GPa melting interval of eclogite plus CO_2 and genesis of silica-under-saturated ocean island lavas. J. Petrol. 47 (4), 647–671.

Demény, A., Sitnikova, M.A., Karchevsly, P.I., 2004. Stable C and O isotope compositions of carbonatite complexes of the Kola Alkaline Province: phoscorite-carbonatite relationships and source compositions. 10, 407-431.

Demeny, A., Ahijado, A., Casillas, R., Vennemann, T.W., 1998. Crustal contamination and fluid/rock interaction in the carbonatites of Fuerteventura (Canary Islands, Spain): a C, O, H isotope study. Lithos 44, 101–115.

Demeny, A., Harangi, S., 1996. Stable isotope studies and processes of carbonate formation in Hungarian alkali basalts and lamprophyres: evolution of magmatic fluids and magma-sediment interactions. Lithos 37, 335–349.

Ding, L.X., Ma, C.Q., Li, J.W., Robinson, P.T., Deng, X.D., Zhang, C., Xu, W.C., 2011. Timing and genesis of the adakitic and shoshonitic intrusions in the Laoniushan complex, southern margin of the North China Craton: implications for post-collisional magmatism associated with the Qinling Orogen. Lithos 126, 212–232.

Dong, Y., Zhang, G., Neubauer, F., Liu, X., Genser, J., Hauzenberger, C., 2011. Tectonic evolution of the Qinling orogen, China: review and synthesis. Asian J. Earth Sci. 41, 213–237.

Doroshkevich, A.G., Viladkar, S.G., Ripp, G.S., Burtseva, M.V., 2009. Hydrothermal REE mineralization in the Amba Dongar carbonatite complex, Gujarat, India. Can. Mineral. 47 (5), 1105–1116.

Du, A., Wu, S., Sun, D., Wang, S., Qu, W., Richard, M., Holly, S., John, M., Dmitry, M.,

2004. Preparation and certification of Re-Os dating reference materials: Molybdenites HLP and JDC. Geostand. Geoanal. Res. 28, 41–52.

Eguchi, J., Dasgupta, R., 2017. CO_2 content of andesitic melts at graphite-saturated upper mantle conditions with implications for redox state of oceanic basalt source regions and remobilization of reduced carbon from subducted eclogite. Contrib. Mineral. Petrol. 172 (2–3), 12.

Exley, R.A., Mattey, D.P., Clague, D.A., Pillinger, C.T., 1986. Carbon isotope systematics of a mantle "hotspot": a comparison of Loihi Seamount and MORB glasses. Earth Planet. Sci. Lett. 78 (2–3), 189–199.

Fan, H.R., Yang, K.F., Hu, F.F., Liu, S., Wang, K.Y., 2016. The giant Bayan Obo REE-Nb-Fe deposit, China: controversy and ore genesis. Geosci. Front. 7, 335–344.

Gao, C., Kang, Q.Q., Jiang, H.J., Zheng, H., Li, P., Zhang, X.M., Li, L., Dong, Q.Q., Ye, X.C., Hu, J., 2017. A unique uranium polymetallic deposit discovered in the Qinling orogenic belt: The Huayangchuan super-large U-Nb-Pb-REE deposit associated with pegmatites and carbonatites. Geochimica 46, 446–455 (in Chinese with English abstract).

Gao, C., Kang, Q.Q., Zhang, X.M., Chen, X.M., Hu, J.P., 2015. Urannium occurrences and carbonatite petrology in Huayangchuan. Geochimica 2, 10–13 (in Chinese with English abstract).

Gaudet, M.A., 2013. Mineralogical Study of Uranium and Niobium Mineralization at the Main Intrusion of the Lofdal Carbonatite Complex, Namibia, Africa.

Gerlach, T.M., McGee, K.A., Elias, T., Sutton, A.J., Doukas, M.P., 2002. Carbon dioxide emission rate of Kilauea Volcano: Implications for primary magma and the summit reservoir. J. Geophys. Res.: Solid Earth 107 (B9) ECV 3-1-ECV 3–15.

Halama, R., McDonough, W.F., Rudnick, R.L., Bell, K., 2008. Tracking the lithium isotopic evolution of the mantle using carbonatites. Earth Planet. Sci. Lett. 265, 726–742.

Halama, R., Vennemann, T., Siebel, W., Markl, G., 2005. The Gronnedal-Ika carbonatite-syenite complex, South Greenland: carbonatite formation by liquid immiscibility. J. Petrol. 46, 191–217.

Hamilton, D.L., Bedson, P., Esson, J., 1989. The behaviour of trace elements in the evolution of carbonatites. Carbonatites: Genesis and Evolution.

Harmer, R.E., Gittins, J., 1998. The case for primary, mantle-derived carbonatite magma. J. Petrol. 39, 1895–1903.

He, S., Li, Z., Hui, X., Guo, J., 2016. $^{40}Ar/^{39}Ar$ Geochronology of biotite in Huayangchuan uranium-polymetallic deposit in Shanxi province and its geological significance. Uranium Geol. 32, 159–164 (in Chinese with English abstract).

Hogarth, D.D., Horne, J.E.T., 1989. Non-Metamict Uranoan Pyrochlore and Uranpyrochlore from Tuff near Ndale, Fort-Portal Area. Uganda. Mineral. Mag. 53, 257–262.

Hou, Z.Q., Liu, Y., Tian, S.H., Yang, Z.M., Xie, Y.L., 2015. Formation of carbonatite-related giant rare-earth-element deposits by the recycling of marine sediments. Sci. Rep. 5, 10231.

Hou, Z., Tian, S., Yuan, Z., Xie, Y., Yin, S., Yi, L., Fei, H., Yang, Z., 2006. The Himalayan collision zone carbonatites in western Sichuan, SW China: petrogenesis, mantle source and tectonic implication. Earth Planet. Sci. Lett. 244, 234–250.

Hu, J., Jiang, S.Y., Zhao, H.X., Shao, Y., Zhang, Z.Z., Xiao, E., Wang, Y.F., Dai, B.Z., Li, H.Y., 2012. Geochemistry and petrogenesis of the Huashan granites and their implications for the Mesozoic tectonic settings in the Xiaoqinling gold mineralization belt, NW China. Asian J. Earth Sci. 56, 276–289.

Hui, X., Cai, Y., He, S., Feng, Z., 2017. Petrologic and geochemical characteristics of carbonatites in Huayangchuan U-Nb-Pb Deposit, Shaanxi province. Geoscience 13, 246–257 (in Chinese with English abstract).

Hui, X., He, S., 2016. Mineralization characteristics of carbonatite veins in Huayangchuan U-ploymetal deposit, Shanxi province. Uranium Geol. 32, 93–98 (in Chinese with English abstract).

Ivanov, K.S., Valizer, P.M., Erokhin, Y., Pogromskaya, O.E., 2010. Genesis of carbonatites of fold belts (exemplified by the urals). Dokl. Earth Sci. 435, 1423–1426.

Javoy, M., Pineau, F., Iiyama, I., 1978. Experimental determination of the isotopic fractionation between gaseous CO_2 and carbon dissolved in tholeiitic magma. Contrib. Mineral. Petrol. 67, 35–39.

Jones, J.H., Walker, D., Pickett, D.A., Murrell, M.T., Beattie, P., 1995. Experimental investigations of the partitioning of Nb, Mo, Ba, Ce, Pb, Ra, Th, Pa, and U between immiscible carbonate and silicate liquids. Geochim. Cosmochim. Acta 59 (7), 1307–1320.

Kalamarides, R.I., 1984. Kiglapait geochemistry VI: Oxygen isotopes. Geochim. Cosmochim. Acta 48, 1827–1836.

Kjarsgaard, B.A., Mitchell, R.H., 2008. Solubility of Ta in the system $CaCO_3$-$Ca(OH)_2$-$NaTaO_3$-$NaNbO_3+/-F$ at 0.1 GPa: implications for the crystallization of pyrochlore-group minerals in carbonatite. Can. Mineral. 46, 981–990.

Klemme, S., Dalpe, C., 2003. Trace-element partitioning between apatite and carbonatite melt. Am. Mineral. 88, 639–646.

Klemme, S., van der Laan, S.R., Foley, S.F., Gunther, D., 1995. Experimentally determined trace and minor element partitioning between clinopyroxene and carbonatite melt under upper mantle conditions. Earth Planet. Sci. Lett. 133, 439–448.

Knudsen, C., 1989. Pyrochlore group minerals from the Qaqarssuk carbonatite complex, Lanthanides, tantalum and niobium. Springer 80–99.

Lai, X.D., Yang, X.Y., Sun, W.D., 2012. Geochemical constraints on genesis of dolomite marble in the Bayan Obo REE-Nb-Fe deposit, Inner Mongolia: implications for REE mineralization. Asian J. Earth Sci. 57, 90–102.

Li, C.Y., Zhang, H., Wang, F.Y., Liu, J.Q., Sun, Y.L., Hao, X.L., Li, Y.L., Sun, W., 2012a. The formation of the Dabaoshan porphyry molybdenum deposit induced by slab rollback. Lithos 150, 101–110.

Li, S.G., Yang, W., Ke, S., Meng, X., Tian, H., Xu, L., He, Y., Huang, J., Wang, X.C., Xia, Q., 2017. Deep carbon cycles constrained by a large-scale mantle Mg isotope anomaly in eastern China. Natl. Sci. Rev. 4 (1), 111–120.

Li, X.H., Long, W.G., Li, Q.L., Liu, Y., Zheng, Y.F., Yang, Y.H., Chamberlain, K.R., Wan,

D.F., Guo, C.H., Wang, X.C., Tao, H., 2010. Penglai zircon megacrysts: a potential new working reference material for microbeam determination of Hf-O isotopes and U-Pb age. Geostand. Geoanal. Res. 34, 117–134.

Liang, J., Ding, X., Sun, X., Zhang, Z., Zhang, H., Sun, W., 2009. Nb/Ta fractionation observed in eclogites from the Chinese Continental Scientific Drilling project. Chem. Geol. 268, 27–40.

Lin, J., Liu, Y., Yang, Y., Hu, Z., 2016. Calibration and correction of LA-ICP-MS and LA-MC-ICP-MS analyses for element contents and isotopic ratios. Solid Earth Sci. 1 (1), 5–27.

Ling, M.X., Liu, Y.L., Williams, I.S., Teng, F.Z., Yang, X.Y., Ding, X., Wei, G.J., Xie, L.H., Deng, W.F., Sun, W.D., 2013. Formation of the world's largest REE deposit through protracted fluxing of carbonatite by subduction-derived fluids. Sci. Rep. 3, 1776.

Liu, H.Y., Montaser, A., Dolan, S.P., Schwartz, R.S., 1996. Evaluation of a low sample consumption, high-efficiency nebulizer for elemental analysis of biological samples using inductively coupled plasma mass spectrometry. J. Anal. At. Spectrom. 11, 307–311.

Liu, Li, X., Zhang, L., An, Z., Xu, L., 2009a. Evaluation of oxygen isotopes in carbonate as an indicator of lake evolution in arid areas: the modern Qinghai Lake, Qinghai-Tibet Plateau. Chem. Geol. 268 (1–2), 126–136.

Li, X., Liu, W., Xu, L., 2012b. Carbon isotopes in surface-sediment carbonates of modern Lake Qinghai (Qinghai–Tibet Plateau): implications for lake evolution in arid areas. Chem. Geol. 300, 88–96.

Liu, Y., Gao, S., Hu, Z., Gao, C., Zong, K., Wang, D., 2009b. Continental and oceanic crust recycling-induced melt–peridotite interactions in the Trans-North China Orogen: U-Pb dating, Hf isotopes and trace elements in zircons from mantle xenoliths. J. Petrol. 51 (1–2), 537–571.

Liu, Y., He, D., Gao, C., Foley, S., Gao, S., Hu, Z., Zong, K., Chen, H., 2015. First direct evidence of sedimentary carbonate recycling in subduction-related xenoliths. Sci. Rep. 5, 1.

Liu, Y., Hu, Z., Gao, S., Günther, D., Xu, J., Gao, C., Chen, H., 2008. In situ analysis of major and trace elements of anhydrous minerals by LA-ICP-MS without applying an internal standard. Chem. Geol. 257, 34–43.

Liu, Y.L., Ling, M.X., Williams, I.S., Yang, X.Y., Wang, C.Y., Sun, W.D., 2018. The formation of the giant Bayan Obo REE-Nb-Fe deposit, North China, Mesoproterozoic carbonatite and overprinted Paleozoic dolomitization. Ore Geol. Rev. 92, 73–83.

Ludwig, K., 2012. User's manual for Isoplot version 3.75–4.15: a geochronological toolkit for Microsoft, Excel Berkley Geochronological Center Special Publication.

Mariano, A.N., 1989. Nature of economic mineralization in carbonatites and related rocks. 149-175.

Martin, L.H.J., Schmidt, M.W., Mattsson, H.B., Guenther, D., 2013. Element partitioning between immiscible carbonatite and silicate melts for dry and H₂O-bearing systems at 1–3 GPa. J. Petrol. 54, 2301–2338.

Mattey, D.P., 1991. Carbon-dioxide solubility and carbon isotope fractionation in basaltic melt. Geochim. Cosmochim. Acta 55, 3467–3473.

Meng, Q.R., Zhang, G.W., 2000. Geologic framework and tectonic evolution of the Qinling orogen, central China. Tectonophysics 323, 183–196.

Mitchell, R.H., 2005. Carbonatites and carbonatites and carbonatites. Can. Mineral. 43, 2049–2068.

Mitchell, R.H., Kjarsgaard, B.A., 2004. Solubility of niobium in the system CaCO₃-CoCaF₂-CoNaNbO₃ at 0.1 GPa pressure: implications for the crystallization of pyrochlore from carbonatite magma. Contrib. Mineral. Petrol. 148, 281–287.

Ning, S., Wang, F., Xue, W., Zhou, T., 2017. Geochemistry of the Baoshan pluton in the Tongling region of the Lower Yangtze River Belt. Acta Geochimica 46, 397–412 (in Chinese with English abstract).

Petruk, W., Owens, D.A.R., 1975. Electron microprobe analyses for pyrochlores from Oka. Quebec. Can. Mineral. 13, 282–285.

Pineau, F., Javoy, M., 1983. Carbon isotopes and concentrations in mid-oceanic ridge basalts. Earth Planet. Sci. Lett. 62, 239–257.

Smith, M.P., Henderson, P., 2000. Preliminary fluid inclusion constraints on fluid evolution in the Bayan Obo Fe-REE-Nb deposit, Inner Mongolia, China. Econ. Geol. 95 (7), 1371–1388.

Song, W., Xu, C., Qi, L., Zhou, L., Wang, L., Kynicky, J., 2015. Genesis of Si-rich carbonatites in Huanglongpu Mo deposit, Lesser Qinling orogen, China and significance for Mo mineralization. Ore Geol. Rev. 64, 756–765.

Song, W.L., Xu, C., Smith, M.P., Kynicky, J., Huang, K.J., Wei, C.W., Zhou, L., Shu, Q.H., 2016. Origin of unusual HREE-Mo-rich carbonatites in the Qinling orogeny, China. Sci. Rep. 6, 37377.

Stein, H., Markey, R., Morgan, J., Du, A., Sun, Y., 1997. Highly precise and accurate Re-Os ages for molybdenite from the East Qinling molybdenum belt, Shaanxi Province, China. Econ. Geol. 92, 827–835.

Sun, S.S., McDonough, W., 1989. Chemical and isotopic systematics of oceanic basalts: implications for mantle composition and processes. Geological Society, London, Special Publications 42, 313–345.

Sun, W., Li, S., Chen, Y., Li, Y., 2002. Timing of Synorogenic Granitoids in the South Qinling, Central China: Constraints on the Evolution of the Qinling-Dabie Orogenic Belt. J. Geol. 110, 457–468.

Sweeney, R.J., 1994. Carbonatite melt compositions in the Earth's mantle. Earth Planet. Sci. Lett. 128, 259–270.

Tappe, S., Steenfelt, A., Nielsen, T., 2012. Asthenospheric source of Neoproterozoic and Mesozoic kimberlites from the North Atlantic craton, West Greenland: New high-precision U-Pb and Sr-Nd isotope data on perovskite. Chem. Geol. 320, 113–127.

Taylor Jr, H.P., Frechen, J., Degens, E.T., 1967. Oxygen and carbon isotope studies of carbonatites from the Laacher See District, West Germany and the Alnö District, Sweden. Geochim. Cosmochim. Acta 31, 407–430.

Thomson, A.R., Walter, M.J., Kohn, S.C., Brooker, R.A., 2016. Slab melting as a barrier to deep carbon subduction. Nature 529 (7584), 76.

Thomsen, T.B., Schmidt, M.W., 2008. Melting of carbonated pelites at 2.5–5.0 GPa, silicate–carbonatite liquid immiscibility, and potassium–carbon metasomatism of the mantle. Earth Planet. Sci. Lett. 267 (1–2), 17–31.

Trofanenko, J., Williams-Jones, A.E., Simandl, G.J., Migdisov, A.A., 2016. The nature and origin of the REE mineralization in the Wicheeda Carbonatite, British Columbia, Canada. Econ. Geol. 111, 199–223.

Tu, X., Zhang, H., Deng, W., Ling, M., Liang, H., Liu, Y., Sun, W., 2011. Application of RESOlution in-situ laser ablation ICP-MS in trace element analyses. Geochimica 40, 83–98 (in Chinese with English abstract).

Veksler, I.V., Dorfman, A.M., Dulski, P., Kamenetsky, V.S., Danyushevsky, L.V., Jeffries, T., Dingwell, D.B., 2012. Partitioning of elements between silicate melt and immiscible fluoride, chloride, carbonate, phosphate and sulfate melts, with implications to the origin of natrocarbonatite. Geochim. Cosmochim. Acta 79, 20–40.

Veksler, I.V., Nielsen, T.F.D., Sokolov, S.V., 1998a. Mineralogy of crystallized melt inclusions from Gardiner and Kovdor ultramafic alkaline complexes: implications for carbonatite genesis. J. Petrol. 39, 2015–2031.

Veksler, I.V., Petibon, C., Jenner, G.A., Dorfman, A.M., Dingwell, D.B., 1998b. Trace element partitioning in immiscible silicate carbonate liquid systems: an initial experimental study using a centrifuge autoclave. J. Petrol. 39 (11–12), 2095–2104.

Viladkar, S.G., Ghose, I., 2002. U-rich pyrochlore in carbonatite of Newania, Rajasthan. Neues Jahrbuch für Mineralogie-Monatshefte 2002, 97–106.

Wang, F., Ge, C., Nie, L., Zhong, G., Noel, C.W., 2017. A new approach to LA-ICP-MS mapping and application in geology. Acta Petrol. Sin. 33, 3422–3436 (in Chinese with English abstract).

Wang, Y., Li, J., Lu, J., Fan, W., 1982. Geochemical mechanism of Nb-, Ta-mineralization during the late stage of granite crystallization. Geochemistry 1 (2), 175–185.

Woolley, A.R., Kjarsgaard, B.A., 2008. Carbonatite occurrences of the world: Map and database. Geological Survey of Canada, Open File 5796.—2008.

Woodard, J., Huhma, H., 2015. Paleoproterozoic mantle enrichment beneath the Fennoscandian Shield: Isotopic insight from carbonatites and lamprophyres. Lithos 236, 311–323.

Xia, X., Song, S., Niu, Y., 2012. Tholeiite-Boninite terrane in the North Qilian suture zone: Implications for subduction initiation and back-arc basin development. Chem. Geol. 328, 259–277.

Xing, C.M., Wang, C.Y., Tan, W., 2017. Disequilibrium growth of olivine in mafic magmas revealed by phosphorus zoning patterns of olivine from mafic–ultramafic intrusions. Earth Planet. Sci. Lett. 479, 108–119.

Xu, C., Campbell, I.H., Allen, C.M., Huang, Z.L., Qi, L., Zhang, H., Zhang, C.S., 2007. Flat rare earth element patterns as an indicator of cumulate processes in the Lesser Qinling carbonatites, China. Lithos 95, 267–278.

Xu, C., Kynicky, J., Chakhmouradian, A.R., Campbell, I.H., Allen, C.M., 2010. Trace-element modeling of the magmatic evolution of rare-earth-rich carbonatite from the Miaoya deposit, Central China. Lithos 118, 145–155.

Xu, C., Kynicky, J., Chakhmouradian, A.R., Li, X., Song, W., 2015. A case example of the importance of multi-analytical approach in deciphering carbonatite petrogenesis in South Qinling orogen: Miaoya rare-metal deposit, central China. Lithos 227, 107–121.

Xu, C., Taylor, R.N., Kynicky, J., Chakhmouradian, A.R., Song, W.L., Wang, L.J., 2011. The origin of enriched mantle beneath North China block: evidence from young carbonatites. Lithos 127, 1–9.

Xu, X.S., Griffin, W.L., Ma, X., O'Reilly, S.Y., He, Z.Y., Zhang, C.L., 2009. The Taihua group on the southern margin of the North China craton: further insights from U-Pb ages and Hf isotope compositions of zircons. Mineral. Petrol. 97, 43–59.

Xue, F., Lerch, M.F., Kroner, A., Reischmann, T., 1996. Tectonic evolution of the east Qinling Mountains, China, in the Palaeozoic: a review and new tectonic model. Tectonophysics 253, 271–284.

Xue, S., Ling, M.X., Liu, Y.L., Sun, W., 2018a. Recycling of subducted carbonates: formation of the Taohuala Mountain carbonatite, North China Craton. Chem. Geol. 478, 89–101.

Xue, S., Xu, Y., Ling, M.X., Kang, Q.Q., Jiang, X.Y., Sun, S.J., Wu, K., Zhang, Z.K., Luo, Z.B., Liu, Y.L., 2018b. Geochemical constraints on genesis of Paleoproterozoic A-type granite in the south margin of North China Craton. Lithos 304, 489–500.

Yang, X.Y., Lai, X.Y., Pirajno, F., Liu, Y.L., Ling, M.X., Sun, W.D., 2017. Genesis of the Bayan Obo Fe-REE-Nb formation in Inner Mongolia, North China Craton: a perspective review. Precambrian Res. 288, 39–71.

Yang, X.Y., Sun, W.D., Zhang, Y.X., Zheng, Y.F., 2009. Geochemical constraints on the genesis of the Bayan Obo Fe-Nb-REE deposit in Inner Mongolia, China. Geochim. Cosmochim. Acta 73, 1417–1435.

Yu, X., 1992. Geological, petrol-mineralogical characteristics and origin of the carbonatites from Huayangchuan, Shaanxi province. Earth Sci.-J. China Univ. Geosci. 17, 151–159 (in Chinese with English abstract).

Yuan, Z.X., Bai, G., Wu, C.Y., Zhang, Z.Q., Ye, X.J., 1992. Geological features and genesis of the Bayan Obo REE ore deposit, Inner-Mongolia, China. Appl. Geochem. 7, 429–442.

Zhang, G., Meng, Q., Yu, Z., Sun, Y., Zhou, D., Guo, A., 1996. Orogenesis and dynamics of the Qinling orogen. Sci. China Ser. D-Earth Sci. 39 (3), 225–234.

Zheng, Y.F., 1990. Carbon-oxygen isotopic covariation in hydrothermal calcite during degassing of CO₂. Miner. Deposita 25 (4), 246–250.